LOCALIZATION OF BIOPSY NEEDLES IN 2D ULTRASOUND IMAGES USING GABOR FILTER

A Thesis

by

Mert Kaya

Submitted to the
Graduate School of Sciences and Engineering
In Partial Fulfillment of the Requirements for
the Degree of

Master Science

in the
Department of Electrical and Electronics Engineering

Özyeğin University
June 2015

Copyright © 2015 by Mert Kaya

LOCALIZATION OF BIOPSY NEEDLES IN 2D ULTRASOUND IMAGES USING GABOR FILTER

Approved by:

Assist. Prof. Özkan Bebek,
Thesis Advisor,
Department of Mechanical Engineering,
Özyeğin University

Assoc. Prof. H. Fatih Uğurdağ,
Department of Electrical and Electronics Engineering,
Özyeğin University

Assist. Prof. Devrim Ünay,
Department of Biomedical Engineering,
Bahçeşehir University

Date Approved: 2 June 2015

To my family

ABSTRACT

Needle Biopsies are common medical procedures to remove tissue samples from the body to be examined for diseases. During these procedures, the needle and its tip are tracked using medical imaging devices to avoid damage to the tissues and to get samples from the targeted site.

Ultrasound (US) is a common imaging method to localize the needles because it does not have any known side effects and provides a larger workspace. However, excessive artifacts and low resolution of the US images make it difficult to localize the needles in the biopsies. A possible solution to this problem is to detect the needle and its tip using an image processing algorithm.

In this thesis, a novel needle localization method is proposed for 2D US images based on the Gabor filter. This method enhances the needle outline to localize the needle, while suppressing other structures in the US images. The needle tip is localized in real-time and the estimation noise is reduced using the Kalman filter. Using the bin packing method, the processing time is reduced by 56%, without a GPU. Also, a simulation study to understand the accuracy of the system within different mediums is conducted.

The proposed needle localization scheme was tested using various phantoms. An external sensor was used to evaluate the accuracy of the needle insertion angle estimation and the needle tip localization methods. The Root mean square (RMS) error of the needle insertion angle was 2.29°; and the RMS error of the needle tip position was 1.17 mm. The results showed that this localization scheme can be used in the US image guided percutaneous needle procedures.

ÖZETÇE

İğne biyopsileri, hastalıkları incelemek için vücuttan doku örnekleri alınarak yapılan yaygın tıbbi işlemlerdir. Bu işlemler sırasında, iğne ve ucu doku hasarından kaçınmak ve hedeflenen yerden örnek almak için tıbbi görüntüleme cihazı ile takip edilir.

Ultrason (US); iğneleri lokalize etmek için kullanılan yaygın bir görüntüleme metodudur çünkü ultrasonun bilinen bir yan etkisi yoktur ve daha büyük bir çalışma alanı sağlar. Ancak, US görüntülerinin düşük çözünürlüğü ve görüntülerdeki yapay olgular, biyopside iğne lokalizasyonu zorlaştırmaktadır. Bu problemin olası bir çözümü iğneyi ve ucunu bir görüntü işleme algoritması ile bulmaktır.

Bu tezde, 2B US görüntülerinde Gabor filtresi tabanlı yeni bir iğne lokalizasyon metodu önerilmektedir. Bu metot görüntüde iğne ana hatlarını artırırken, diğer yapıları sönümlemektedir. İğne ucu gerçek zamanda lokalize edilmiştir ve tahmin gürültüsü Kalman filtresi kullanılarak azaltılmıştır. Önerilen metodu gerçek zamanda çalıştırmak için kutu paketleme yöntemi kullanılmıştır ve işlem süresi GPU kullanılmadan %56 azaltılmıştır. Ayrıca sistemin farklı ortamlardaki hassasiyetini anlamak için bir simülasyon çalışması yapılmıştır.

Önerilen iğne lokalizasyon planı çeşitli fantomlar kullanılarak test edilmiştir. İğne giriş açısı tahmin ve iğne ucu lokalizasyon metotları harici bir sensör kullanılarak değerlendirilmiştir. İğne giriş açısı tahminindeki kök ortalama kare hatası 2.29° ve iğne ucunun pozisyondaki kök ortalama kare hatası 1.17 mm olarak ölçülmüştür. Deney sonuçları önerilen lokalizasyon planının US görüntü rehberliğinde yapılan deri altı biyopsi uygulamalarında kullanılabileceğini göstermiştir.

ACKNOWLEDGEMENTS

First of all, I thank Professor Özkan Bebek for accepting me as his master student. I am very grateful for his guidance and support during my master study. He tread me very kind. He spent lots of time on reading my papers and this thesis. I learned a lot from him about how to make research and how to write academic papers better. I am thankful for his encouragement, help, and patience which enabled me to complete this thesis.

My thanks also go to the other members of thesis defence committee, Professor H. Fatih Uğurdağ and Professor Devrim Ünay. They support me throughout my bachelor's and master's education. They helped me without any hesitation. I am so glad to see them in my thesis defence committee.

I also want to thank all the members of the Ozyegin Robotics Lab members for their friendship. We worked together nights and days and shared lots of good times in the Robotics Lab.

Special thanks go to my family with my deepest gratitude. They supported me to complete my thesis from every angle. They made a lot of sacrifices during my educational life. I am so grateful for everything.

This research was done in the Robotics Laboratory at Özyeğin University; supported by the Scientific and Technical Research Council of Turkey (TÜBITAK) under Grant No. 112E312.

TABLE OF CONTENTS

DEDICATION . . . . . **iii**

ABSTRACT . . . . . **iv**

ÖZETÇE . . . . . **v**

ACKNOWLEDGEMENTS . . . . . **vi**

LIST OF TABLES . . . . . **ix**

LIST OF FIGURES . . . . . **x**

I INTRODUCTION **1**

1.1 Thesis Contribution 2

1.2 Thesis Outline 3

II RELATED WORKS IN THE LITERATURE **4**

III TISSUE MIMICKING MATERIALS FOR US PHANTOMS . . **8**

3.1 Acoustic Properties of Phantoms 9

3.2 Water Medium as Phantom 14

3.3 Gelatine Based Phantoms 16

3.4 Agar Based Phantom 18

3.5 Agar-Gelatine Based Phantom 19

3.6 Evaporated Milk Based Phantom 23

3.7 Polyvinyl Alcohol Based Phantom 24

3.8 Paraffin Based Phantom 25

3.9 Silicon Based Phantom 26

3.10 Magnesium Silicate Based Phantom 26

IV NEEDLE LOCALIZATION IN 2D ULTRASOUND IMAGES . . **28**

4.1 Gabor Filter 31

4.2 Estimation of Needle Insertion Angle 31

4.2.1 Estimation of the Needle Insertion Angle from a single US image 32

4.2.2 Estimation of the Needle Insertion Angle in Frame Sequences 36
4.3 NEEDLE AXIS LOCALIZATION 39
4.3.1 Image Binarization 39
4.3.2 Line Detection & Region of Interest 42
4.3.3 Parameter Tuning for Otsu's Thresholding 43
4.4 Location Estimation of the Needle Tip 46
V REAL-TIME NEEDLE TIP LOCALIZATION 54
5.1 Kalman Filter for Smoothing Estimation Noise 54
5.2 Needle Tip Tracking Simulation 57
5.3 Bin Packing 60
VI EXPERIMENTAL RESULTS 64
6.1 Experimental Setup 64
6.1.1 Biopsy Robot - OBR 64
6.1.2 US Machine 65
6.1.3 Phantom 65
6.1.4 Execution Time 66
6.2 Needle Localization Results 66
6.2.1 Simulation Results 66
6.2.2 Experimental Results 67
VII CONCLUSION 70
REFERENCES 73

LIST OF TABLES

1 Acoustic properties of tissues 10

2 Acoustic and mechanical properties of agar-gelatine phantom 23

3 Processing time of each process in Fig. 26 62

LIST OF FIGURES

1 Configuration #1: Experimental setup used in measuring speed of sound and attenuation coefficient. 11

2 Configuration #2: Experimental setup used in measuring speed of sound and attenuation coefficient. 12

3 2D US image of the needle in the distilled water. 15

4 2D US image of the needle in the distilled water-ethanol mixture. . . 16

5 2D US image of the needle in the gelatine phantom. 18

6 2D US image of the needle in the agar phantom. 20

7 2D US image of the needle in the agar-gelatine phantom. 22

8 Comparison of the proposed localization method with other localization methods in the literature. 29

9 Flowchart of the proposed needle localization algorithm. 30

10 The output of the Gabor filter bank using the proposed line filter . . 33

11 The US and needle coordinate systems 34

12 The order of the needle insertion angle estimation and detection in 2D US images. 35

13 The order of the needle insertion angle estimation and detection in 2D US frame sequences. 38

14 The output of the Gabor filter based needle axis localization. 41

15 Needle region of interest coordinates. 43

16 Results of the proposed entropy-based parameter tuning method. . . 46

17 3D probability map of the needle's tip overlaid on the 2D US images of the agar and agar-gelatin based phantoms 50

18 3D probability map of the needle's tip overlaid on the 2D US images of the water-ethanol phantom and water medium 51

19 The output of the Gabor filter based needle tip estimation. 52

20 Three dimensional probability map of the needle's tip overlaid on the two dimensional US image. 53

21 Kalman Filter Implementation 55

22 Results of the proposed needle tip localization algorithm. 56

23 Simulation snapshots of the needle tip tracking 58

24 Needle tip estimation error versus time. 59

25 Snapshots of the tissue deformation while the needle is inserted. . . . 60

26 Schematic representations of sequential and bin packing methods. . . 63

27 View of 2D US guided 5-DOF robotic system for percutaneous needle procedures. 65

28 Processing time of the sequential and the bin packing methods are presented as histogram plot. 67

29 Experimental setup to evaluate the accuracy of the proposed needle localization method. 68

CHAPTER I

INTRODUCTION

Percutaneous needle procedures, such as biopsy or drug delivery, are frequently performed medical operations. The needle placement plays a significant role in the success of the operations [1]. If the needle is placed inaccurately, the tissue sample from an incorrect location might be collected, and repeated insertions might damage the tissue leading to hemorrhage. In order to improve the placement accuracy and reduce such failures, the needle path has to be predetermined and the needle tip should be tracked.

Percutaneous needle procedures are performed with the help of medical imaging, including magnetic resonance imaging (MRI), computed tomography (CT), fluoroscopy and ultrasound (US). MRI provides high quality images for biopsy operations, however custom needles are required for needle localization since they are ferromagnetic. Also, MRI does not provide enough workspace for all operations. CT and fluoroscopy imaging can be used but they are harmful due to radiation. In addition, similar to MRI, the workspace of CT is limited. US imaging, on the other hand, does not have any known side effects. The needle can be tracked with a very small probe. However, visualization of the needle can be challenging due to poor image quality. US images contain undesirable artifacts and reverberation effects. Therefore, the visibility of the needle, especially its tip, is poor in the images. At this point, image processing algorithms can be used to reduce these artifacts and increase the visibility of the needle to localize the needle axis and track its tip.

This thesis presents a novel image processing method for automated needle localization in 2D US images. The proposed method uses a Gabor filter to segment

the needles in US images. The Gabor filtered images are then binarized with an automatic parameter tuning method and the needle trajectory is obtained using line fitting. Finally, location of the needle tip is estimated using the probabilistic mapping method. In order to perform the method in real time, the bin packing method is used. Also, in order to test the system with imaging faults and tissue deformations, needle tip tracking simulations are performed. The effectiveness of the method is shown using different types of tissue phantoms and water medium.

1.1 Thesis Contribution

This work has led several contributions in the needle localization in 2D US images. Following summarizes the contributions with the corresponding publications:

Gabor filter is proposed to segment needle pixels in ICRA2014 article [2]. Gabor filter enhances the needle pixels while suppressing other structures like artifacts. Hence, Gabor filter produces much better results compared to other filtering methods in the literature while significantly filtering the artifacts. Also, in this study, needle insertion angle estimation method without known priori is proposed.

An entropy based parameter tuning for Otsu's threshold and probability mapping method to find location of the needle tip have been proposed in IST2014 article [3]. It was observed that when the needle segmentation threshold value generated by Otsus method was multiplied with a pre-tuned constant parameter (α), the Gabor-based line filtering method became more robust, and the processing time was reduced. In this study, an entropy based automated parameter tuning method to dynamically adjust the α parameter is proposed. Also, a probability mapping for the needle tip estimation is created using the Gabor filter output, which shows possible needle tip locations.

Real time needle tip tracking is also proposed, where the needle axis is localized using a Gabor filter in ICAR2015 article [4]. In this study, the needle tip is tracked

using 2D US imaging, and additionally, the needle tip estimation noise is smoothened using a Kalman filter. The processing time of the proposed localization method is reduced by approximately 56% using the bin packing method, so that the algorithm can be executed in real time. Also, the needle tip tracking simulation is presented to test the Kalman filter performance under image misalignment and tissue deformations.

1.2 Thesis Outline

This thesis consists of seven chapters. It is organized as follows. In the current chapter, the problem is introduced and our contribution to needle localization in 2D US images are discussed. Related works in literature done on needle and its tip localization in US images are given in Chapter II. Chapter III explains tissue mimicking materials and phantoms preparation methods. It further outlines acoustical properties of human tissue and phantoms. Chapter IV presents Gabor filter based needle localization algorithm in 2D Images. The real time needle tip localization is described in Chapter V. In Chapter VI, experimental and simulation results are given. Finally, Chapter VII concludes the thesis by summarizing the contributions and experimental results.

CHAPTER II

RELATED WORKS IN THE LITERATURE

In literature, there are many studies done on needle and needle tip localization. The following summarizes the work conducted on developing needle localization algorithms.

Draper *et al.* [5] used variance mapping to discriminate the needle from the background. They used a user defined thresholding technique and then principal component analysis (PCA) to localize the needle axis and its tip. Ding and Fenster [6] used fast implementation of Hough Transform based on course-fine search to segment the needle in 2D US images. Their approach decreased the computational time and can segment the biopsy needle in real time. Cheung and Rohling [7] enhanced the needle visibility in 2D US images by steering the US beam. The needle was localized using Hough transform and specific beam patterns were used to maximize the reflections from the needle. Barva *et al.* [8], [9] localized curvilinear objects in 3D US images. 3D US images were converted to binary images with empirically determined threshold values and then curve fitting was applied to localize the objects.

Okazawa *et al.* [10] used Hough transform and coordinate transform to localize curved needles under 2D US images. Rough insertion angle was supplied by the user for needle segmentation. Novotny *et al.* [11] and Stoll *et al.* [12] used passive markers for tracking surgical instruments in 3D US images. Markers' position were computed from a 3D US image then the position and the orientation of the surgical instrument was determined, and GPU was used to track the instrument in real time. Neshat and Patel [13] modeled curved needles with Bezier polynomials. The coefficients of the polynomial were estimated using Radon Transform. In order to run the algorithm

in real time, they implemented their curved needle segmentation code on a GPU. Fronheiser *et al.* [14] and Adebar *et al.* [15] tracked needle with 3D color doppler US device. They vibrated the needle at high frequency with a piezoelectric buzzer. RF and color doppler filters were used to detect the tip of the surgical devices from US images.

Dong *et al.* [16] proposed a framework for real time needle localization in highly noisy 2D US images. They used level set and partial differential equation to localize and track the biopsy needle. Uhercik *et al.* [17] and Zhao *et al.* [18] used Frangi's vessel segmentation algorithm [19] to filter lines in 3D US images. The axis of the needle was determined by a robust model fitting random sample consensus (RANSAC) algorithm. Aboofezali *et al.* [20] segmented curved needles in 3D US images using an anti isotropic filter. This process reduced speckles in the image and the remaining speckles were reduced with a spatial contrast enhancement filter. 3D images were projected to 2D using ray casting and then Hough transform was applied to detect the curvilinear needle.

Wen *et al.* [21] detected the brachytherapy seeds in 3D US images. They used reflected power images instead of conventional B-mode US images. After the seed insertion was detected with Hough transform, the seeds were segmented and localized in priorly determined local search space. Ayvaci *et al.* [22] tracked the biopsy needle in 2D transrectal US images. Needle pixels in the image were mapped using prior knowledge of the needle's position, the image background model, and the US probe stability. Cao *et al.* [23] proposed automated catheter detection in 3D images. A likelihood map was generated according to the physical model of the catheter. The map was projected onto a single image plane with respect to the maximum intensity approach to detect catheter faster.

Vrooijink *et al.* [24] developed a robotic system to track the needle tip in three dimensions within 2D US images. The needle was inserted by a motorized device, US

probe was servoed by a positioning device and the robotic system provided feedback for the image guidance. The specific pattern of the needle in US imaging, known as the comet tail artifact (CTA) was used to detect the needle tip. After thresholding and morphological operations, the CTA pattern was detected and the needle tip was localized. Chatelain *et al.* [25] proposed a method to detect and track a manually inserted needle in real-time using a 3D US probe mounted on a 6-DOF robotic arm. The needle insertion was detected using the geometric median and the volume intensity differences. Prospective needle pixels were obtained using the volume intensity differences and the needle axis was localized using RANSAC. A Kalman filter was applied to track the needle more accurately.

Renfrew *et al.* [26] proposed a framework for active localization of the needles and targets in image guided robotic interventions. Their approach was based on the active localization of the needles and the targets by maximizing information. A particle filter was used to estimate the needle and the target states. They validated their proposed localization approach with simulation. Mathiassen *et al.* [27] used the second order derivative of a 2D Gaussian function and the frame difference information of the sequential frames to estimate the needle tip in 2D US images. The accuracy of the system was measured using an optical tracker. Beigi and Rohling [28] located a needle in a 2D US image sequence using motion information. After the motion was detected, the needle axis was obtained using polynomial fitting and Hough transform on the pixel extracted from the difference image. The last detected point along the needle axis in the difference image was considered as the needle tip.

This thesis introduces a new needle localization method in 2D US images. Specifically, the Gabor filter is applied to detect the needle, which has not been used in needle localization studies with US imaging before. The Gabor filter produces much better results compared to other filtering methods because it enhances the needle's pixel better. This thesis also presents automatic parameter tuning method optimizes

the threshold value that is used by the Otsu's thresholding technique to automatically binarize the ultrasound image. A probability map is created to estimate the needle tip location using the Gabor filtered image and the binarized image. The needle tip is also tracked using 2D US imaging, and additionally, the needle tip estimation noise is smoothened using a Kalman filter. The processing time of the proposed localization method is reduced by approximately 56% using the bin packing method, so that the algorithm can be executed in real time. Also, the needle tip tracking simulation is presented to test the Kalman filter performance under image misalignment and tissue deformations.

CHAPTER III

TISSUE MIMICKING MATERIALS FOR US PHANTOMS

Ultrasound phantoms simulate acoustical properties of the human tissue. They provide realistic medium for US imaging and they are used for several purposes. First, phantoms are used to train sonographers [29]. US imaging is widely used in medical diagnosis. However, US images are inherently noisy and their resolution are low. Hence, it is not easy to recognize patterns in the US images. The sonographers need to practice to learn scanning techniques, anatomical details, feature of artifacts and probe manipulation. But, it is not always feasible to train sonographers with patients or cadavers. US image of actual clinical conditions can be closely simulated with phantoms. Hence, it provides realistic training medium for sonographers. Second, phantoms are used to calibrate US machines and evaluate the quality of US image quality [30]. Phantoms are used for these purposes are called calibration phantoms. There are not any anatomical structures in calibration phantoms. Certain sized objects are embedded in these phantoms at known positions. Also, acoustical properties of the objects are known. The important parameters of the US machines are obtained from calibration phantom image to evaluate US machines performance. Third, phantoms are used as test medium for percutaneous needle procedures, such biopsy and drug delivery. In these procedures, US imaging provides visual feedback. Operators need to practice and train to improve their hand-eye coordination skills to reach target before performing it on a patient. Hence, needle can be placed correctly and unwanted side effects can be prevented. Phantoms provide test mediums to determine needle trajectory and track needle tip in US images [31]. With phantoms, organs, tissues, and cysts can be mimicked and also it is cost effective.

There are commercially available phantoms. Commercial phantoms provide very realistic images for US imaging. They are capable of mimicking whole human body in US imaging. They are made from rubber so they are very durable. However, they are very expensive so they are generally used in calibrating US machine and observing anatomical details in US images. Phantoms can be also prepared in laboratory with tissue mimicking materials (TMM). Their acoustical properties can be controlled and they are capable of mimicking desired human tissue. They are generally used in needle insertion experiments.

In this thesis, homogenous and heterogenous phantoms were used during the needle insertion experiments. Homogenous phantoms were used to assess the detectability of the needles in US images while heterogenous phantoms were used to observe the needles under the realistic conditions. Thus, images from different backgrounds are collected using the phantoms. A database was created using the collected images to test the proposed localization method in various backgrounds and under the realistic conditions. All of the phantoms used in this study were produced in the laboratory using tissue mimicking materials. In this work, agar, gelatin, evaporated milk, polyvinyl alcohol, paraffin, silicon, and magnesium silicate were used as tissue mimicking materials to produce US phantom. In the rest of the chapter, acoustic properties of phantoms and preparation of phantoms using these substitutes are explained.

3.1 Acoustic Properties of Phantoms

Ultrasound image is created by firstly sending high frequency sound waves into tissue using ultrasound transducer. Then, ultrasound transducer acts as a receiver and collects the reflected sound waves (echoes) from the tissue. These echoes are analyzed and the acoustical properties of the tissue along sound path is extracted. The most important acoustical properties for US image reconstruction are speed of sound,

Table 1: Acoustic properties of tissues (Table reproduced from [33])

Material	Speed of Sound (m/s)	Density (kg/m^3)	Attenuation Coefficient $(dB.(cm.MHz)^{-1})$	Acoustic Impedance $MRayl$
Soft Tissue	1561	1043	0.54	1.63
Liver	1595	1060	0.5	1.69
Breast	1510	1020	0.75	1.54
Fat	1478	950	0.48	1.40
Blood	1584	1060	0.2	1.68
Brain	1560	1040	0.6	1.62
Water	1480	1000	0.0022	1.48
Bone, Cortical	3476	1975	6.9	7.38
Bone, Trabecular	1886	1055	9.94	1.45
Muscle	1547	1050	1.09	1.62
Tendon	1670	1100	4.7	1.84
Marrow	1435	-	0.5	-
Air	330	1.2	-	0.0004

attenuation coefficient, acoustic impedance, and back scattering power [32]. These properties change according to tissue type (see table 1). Hence, contrast is obtained and intensity of echoes are interpreted using these acoustical properties.

Phantoms mimic the desired human tissue in US imaging. For realistic mimicking, acoustical properties of phantom must match with acoustical properties of desired tissue. In general, acoustic impedance, speed of sound and attenuation coefficient of phantom are evaluated. These acoustical properties are measured with water tank experiment. Water tank experiment consists of ultrasound transducer, hydrophone (microphone used in underwater to listen or record underwater sound) and distilled water. Transducer is triggered by signal generator and US beam is sent into phantom. The passing signal through phantom is collected by hydrophone and collected signal is amplified. Then, amplified signal is acquired with data acquisition and acoustical properties of phantoms is calculated. There are two types of water tank setup. The main difference between them position of hydrophone. In Configuration #1, ultrasound transducer and hydrophone are sperate units and they are placed opposite to

each other (Fig. 1). Phantom is placed between them. In Configuration #2, ultrasound sensor can act as both transducer and hydrophone. The phantom placed at the bottom of tank (Fig. 2). In this configuration, plane reflector is placed between phantom and bottom of tank to maximize the reflection. Hence, reflection time is determined more certainly. Flat glass is generally used as plane reflector because it can reflect sound waves with -9 dB.

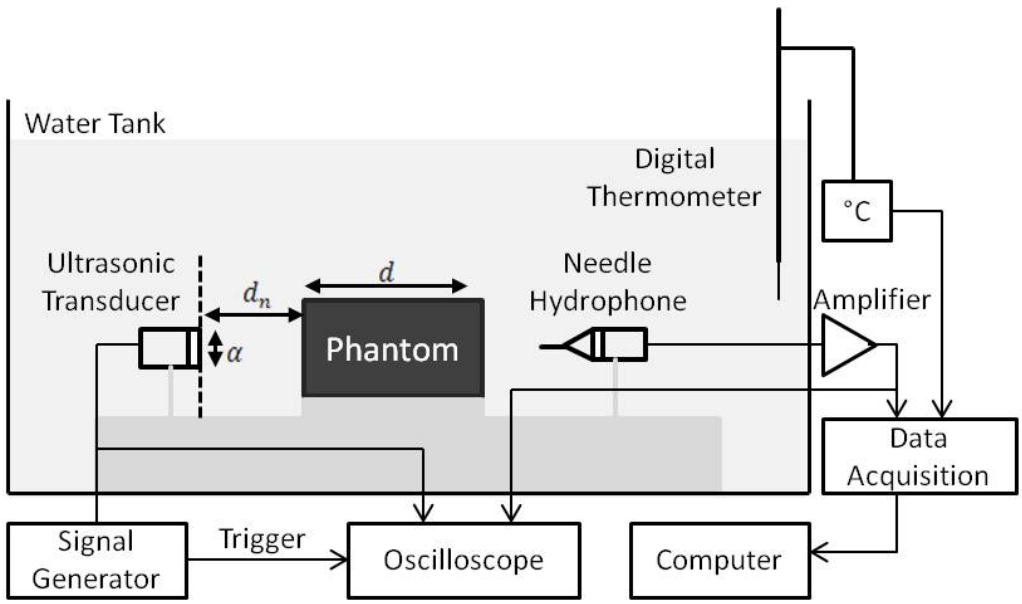

Figure 1: Configuration #1: Experimental setup used in measuring speed of sound and attenuation coefficient. Figure reproduced from [34].

In the water tank experiments, water is the reference medium; the acoustical properties of phantom are calculated using acoustical properties of water. Speed of sound (c) in phantom is calculated for configuration #1, #2 as follows:

$$c = c_w \left(1 + \frac{c_w \triangle t}{d}\right)^{-1} \quad and \quad c = c_w \left(1 + \frac{c_w \triangle t}{2d}\right)^{-1} \tag{1}$$

where c_w is the speed of sound in water, d is phantom thickness of phantom, and $\triangle t$ is time shift in wave propagation. It is note that speed of sound in distilled water changes according to its temperature. Hence, temperature of the distilled water is measured with digital thermometer and speed of sound in distilled water is obtained.

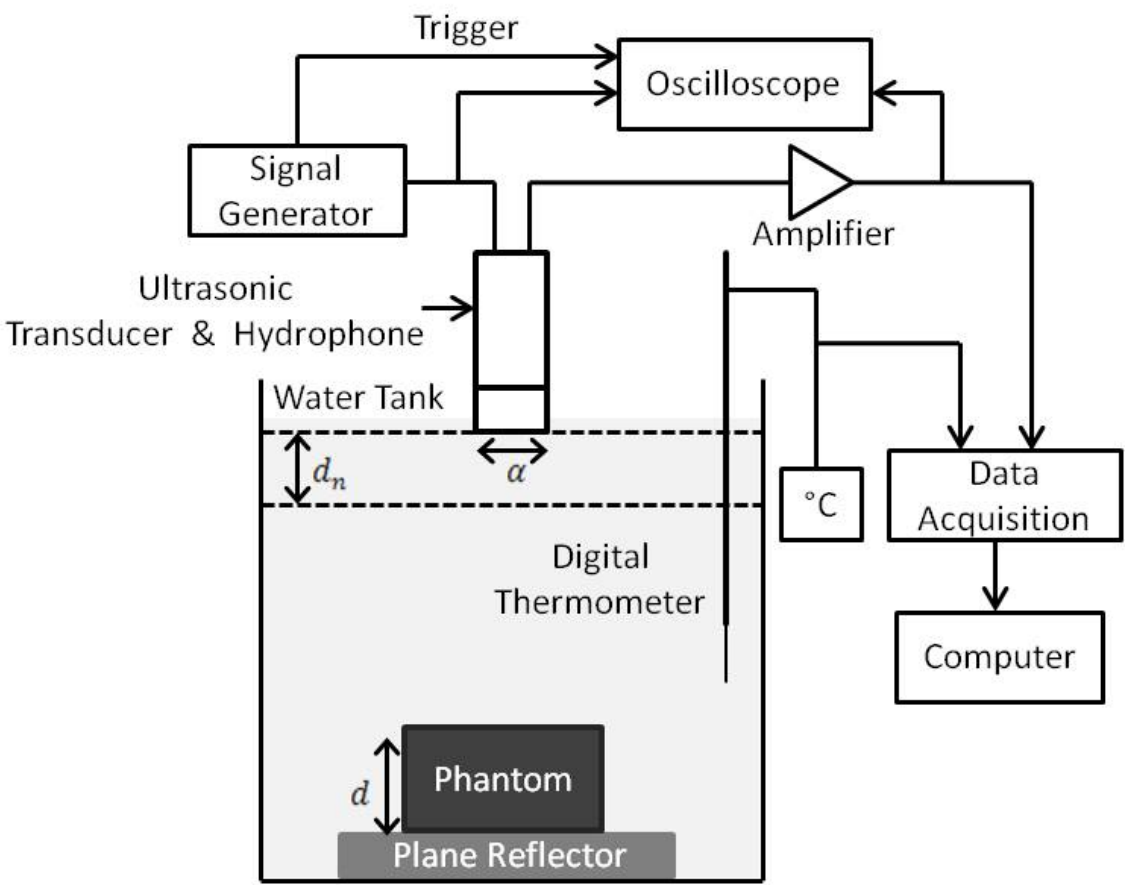

Figure 2: Configuration #2: Experimental setup used in measuring speed of sound and attenuation coefficient. Figure reproduced from [35].

Attenuation coefficient is quantifying phantom or tissue according to how transmitted sound wave amplitude decreases as a frequency (f). It is measured firstly sending sound wave to hydrophone before placed phantom and power of receiving signal ($A_o(f)$) is calculated using fast Fourier transform (FFT) analysis. Then, phantom is placed between transducer and hydrophone and the power of receiving signal ($A(f)$) is calculated. These steps are applied with sending sound wave with different frequencies into phantom or tissue. Attenuation coefficient is calculated as follows:

$$a(f) = -\frac{10}{d}\log_{10}\left(\frac{A(f)}{A_{o(f)}}\right) \tag{2}$$

The attenuation coefficient is measured in units of decibel per cm ($dB.(cm)^{-1}$).

The unit is independent from frequency. Hence, for each frequency, different attenuation coefficient is obtained. However, attenuation coefficient is linearly dependent to frequency of ultrasound beam. If the attenuation coefficient in unit of $(dB.(cm)^{-1})$ is divided by frequency, attenuation coefficient become invariant to frequency. Hence, the attenuation coefficient is measured in units of $(dB.(cm.MHz)^{-1})$. in ultrasound imaging.

Acoustic impedance is the opposition of medium (phantom, tissue) to acoustical flow. The unit of acoustic impedance is rayl. Acoustical impedance (z) is calculated by multiplication of density of phantom (p_s) and speed of sound in phantom (c):

$$z = p_s.c \tag{3}$$

Back scatter power is the power of reflected sound waves from medium (tissue, phantom). It depends on frequency of sound wave (f) and its unit is decibel (dB). Back scattering power is measured with a different setup used for measuring speed of sound and attenuation. In order to measure back scattering power, the reflected signal from front face of phantom and reflector is captured. Hence, transducer focus is narrowed and driver voltage is increased. These adjustments minimize reflections from the front face of the sample phantom and increase the signal to noise ratio of the backscattered signal. It is measured firstly sending sound wave before placed the phantom and power of reflected wave is calculated ($I_o(f)$). Then, phantom is placed between transducer and plane reflector and the power of reflected signal ($I(f)$) from phantom is calculated. In order to calculate the signal power, the reflected signal is firstly filtered with Hamming window because there is spectral leakage. Then, power of filtered signal is calculated using Welch method. Back scatter power (μ) is calculated as follows:

$$\mu(f) = -10 \log_{10} \left(\frac{I(f)}{I_o(f)} \right) \tag{4}$$

In the water tank experiment setup, there should be minimum distance between ultrasound transducer and phantom. If the phantom placed near than minimum distance, ultrasound wave do not scatter. The minimum distance (d_n) depends on aperture size of ultrasound transducer (a) and wavelength of ultrasound wave. For example, if the temperature of distilled water in tank is $25°C$ (the speed of sound in water at this temperature is 1484 m/s) and frequency of ultrasound transducer is 8 MHz, the wavelength of sound wave:

$$\lambda = \frac{c_w}{f} = \frac{1484\, m/s}{8 \times 10^{-6}\, 1/s} = 1.855 \times 10^{-4}\, m. \tag{5}$$

The minimum distance between phantom and ultrasound transducer:

$$d_n = \frac{(a/2)^2}{\lambda} = \frac{(70\, mm)^2}{0.1855\, mm} = 26,4\, mm. \tag{6}$$

3.2 Water Medium as Phantom

Water is used as test medium in ultrasound imaging. The speed of sound and attenuation coefficient are 1480 m/s and 0.022 $dB.(cm.MHz)^{-1}$, respectively. According to these values, speed of sound is in the desired level but the attenuation coefficient is very low to mimic soft tissue in ultrasound images. Lack of attenuation in water provides black and homogenous background for US images. Hence, the best appearance of the objects like surgical tools in ultrasound images are obtained. 2D US images of the biopsy needle in the distilled water are shown in Fig. 3.

Speed of sound in water changes according to distill water temperature. There is a direct proportion between them. In our experiments, the temperature of water was close to room temperature and it was rested about 8-10 hours before the experiment to eliminate air bubbles. The speed of sound can be also controlled with alcohols. The most frequently used one is ethanol. The speed of sound in water-ethanol mixture can be calculated as follows [36]:

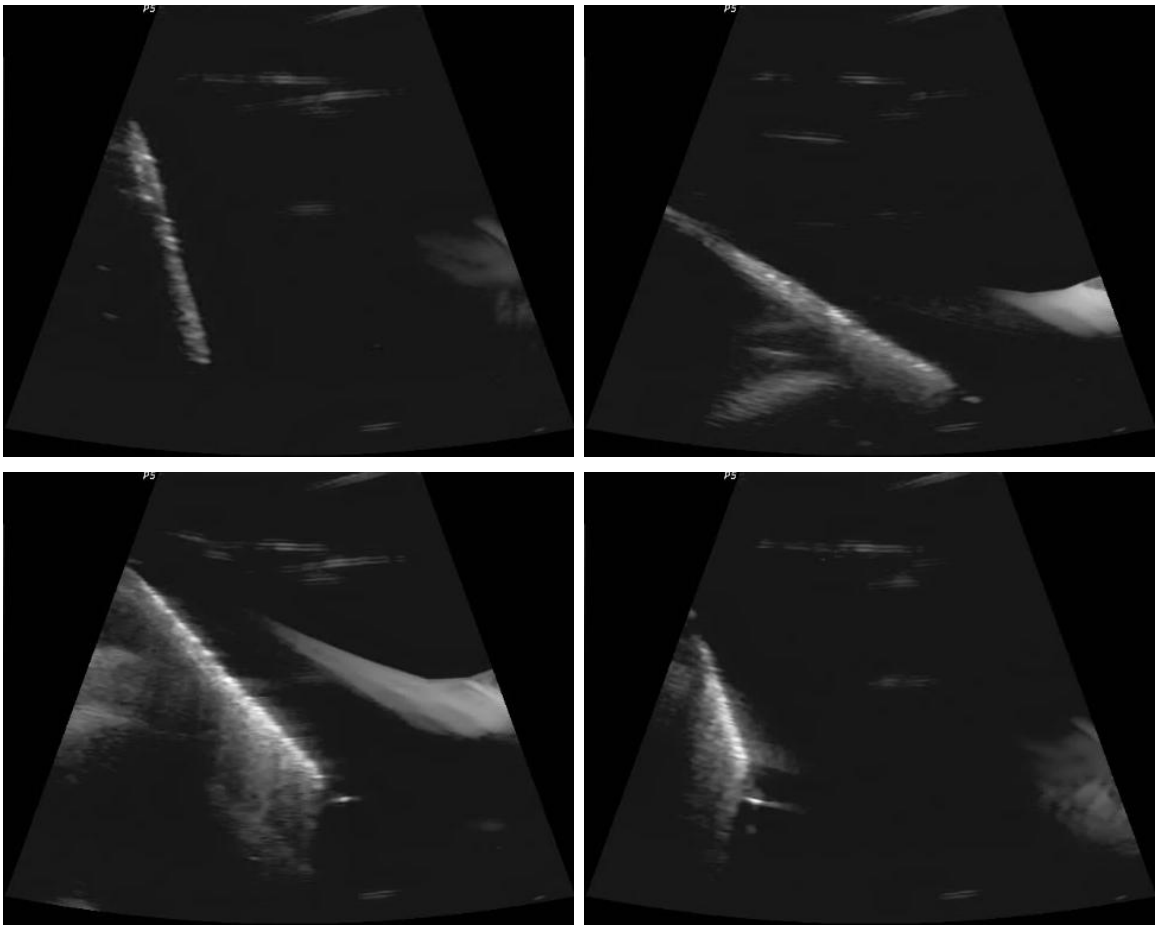

Figure 3: 2D US image of the needle in the distilled water.

$$
\begin{aligned}
C_{we} = {} & 1606.9 - 121.7E + 121.7W - 4.7T + 245.5EW - 1.1ET \\
& + 1.1WT - 245.5E^2 - 245.5W^2 - 0.01T^2 + 521.8EW^2 \\
& - 521.8WE^2 + 0.003ET^2 + 2.9ET - 0.003WT^2 + 5.6W^2T.
\end{aligned} \tag{7}
$$

where C_{we} is the speed of sound in water-ethanol mixture, T is the temperature of mixture, E and W are the percentages of ethanol and water in the mixture.

In our experiments, speed of sound in water-ethanol mixture was calculated 1560 m/s. According to equation 7, the percentage of ethanol in the mixture was calculated 7.2%. ($E = 0.072$, $W = 0.9993$, and $T = 25°C$). In order to produce 1 lt water-ethanol mixture 7.2 ml ethanol and 928 ml distilled water are mixed in a beaker. The

mixture is stirred with magnetic stripper about 30 min. 2D US images of the biopsy needle in the distilled water-ethanol mixture are shown in figure 4.

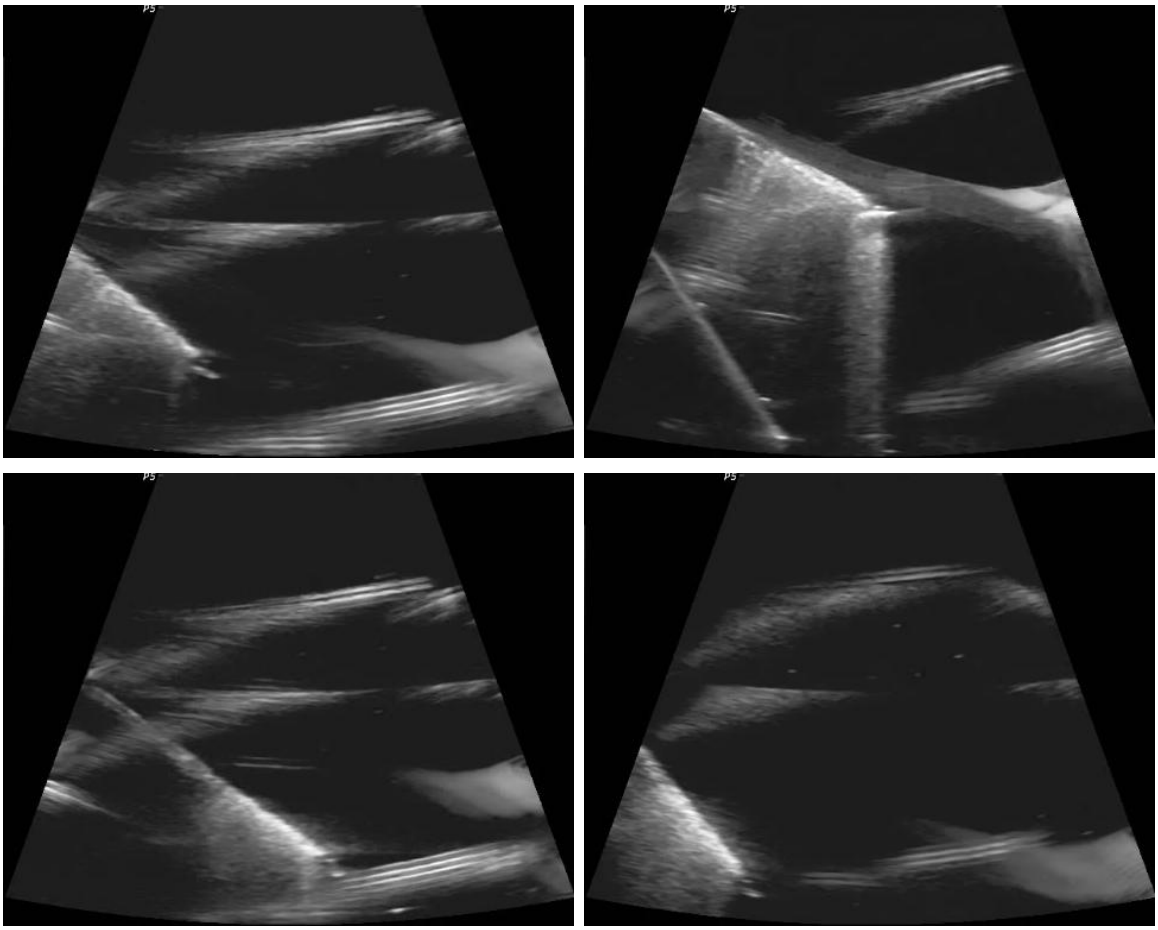

Figure 4: 2D US image of the needle in the distilled water-ethanol mixture.

3.3 Gelatine Based Phantoms

Gelatine is one of most commonly used materials to prepare phantom. Gelatine based phantoms can realistically mimic human tissue in ultrasound imaging. Also, it is easy to prepare and their cost is low. The speed of sound and attenuation coefficient in gelatine and water mixture are 1520 m/s and 0.12 $dB.(cm.MHz)^{-1}$, respectively [33].

In order to prepare 1 lt gelatin phantom, following steps are applied. Gelatin dissolves at $60°C$ so 920 ml distilled is heated to $60°C$. Then, 80 g gelatin is added and stirred until its color become transparent. The mixture is cooled under stirring to

$25°C$. It is note that gelatin based phantoms do not have resistance to microbiological attacks. Therefore, 5 ml benzalkonium chloride is added and mixed it at $25°C$ to preserve the phantom. Finally, the mixture is poured into polyurethane cap and rested 15 minutes to eliminate bubbles. It is cooled in refrigerator at least 8 hours. The main disadvantage of gelatin based phantoms is that they are thermally unstable [37], [38]. After it is extracted form container, dehydration occurs and acoustical properties change. Thermal stability can be increased with calcium chloride ($CaCl_2$) treatment. After the solid gel is extracted form mold, it is suspended in 0.5M $CaCl_2$ 24 hours. Thermal stability can be also increased with adding formalin (37 % formaldehyde) [39]. In phantom preparation, 3 ml formalin is added to gelatin mixture at $37°C$. Adding formalin increases the melting point of phantom to $78°C$ [39].

2D US images of the biopsy needle in the gelatin phantom prepared with this recipe are shown in figure 5. As seen from picture, gelatin-water mixture provide black homogeneous background for ultrasound imaging because attenuation coefficient is low. For realistic tissue mimicking, attenuation coefficient must be increased. The attenuation coefficient can be controlled with metamucil or graphite. It was reported that attenuation coefficient can be increased with metamucil until 0.54 $dB.(cm.MHz)^{-1}$ [40] and it can be increased with graphite until 1.45 $dB.(cm.MHz)^{-1}$ [41]. In our experiments, soft tissue has been mimicked. Hence, the attenuation coefficient must be close to 0.54 $dB.(cm.MHz)^{-1}$. In order to increase attenuation of gelatin, either 4% metamucil or 0.073 g/cm^3 graphite can be added to gelatin-water mixture.

The speed of sound in gelatine can be also controlled with n-propanol. It can be increased until 1650 m/s. The speed of sound changes linearly with respect to percentages of n-propanol in the mixture. Adding each 1% n-propanol increases the speed of sound by approximately 5 m/s [41].

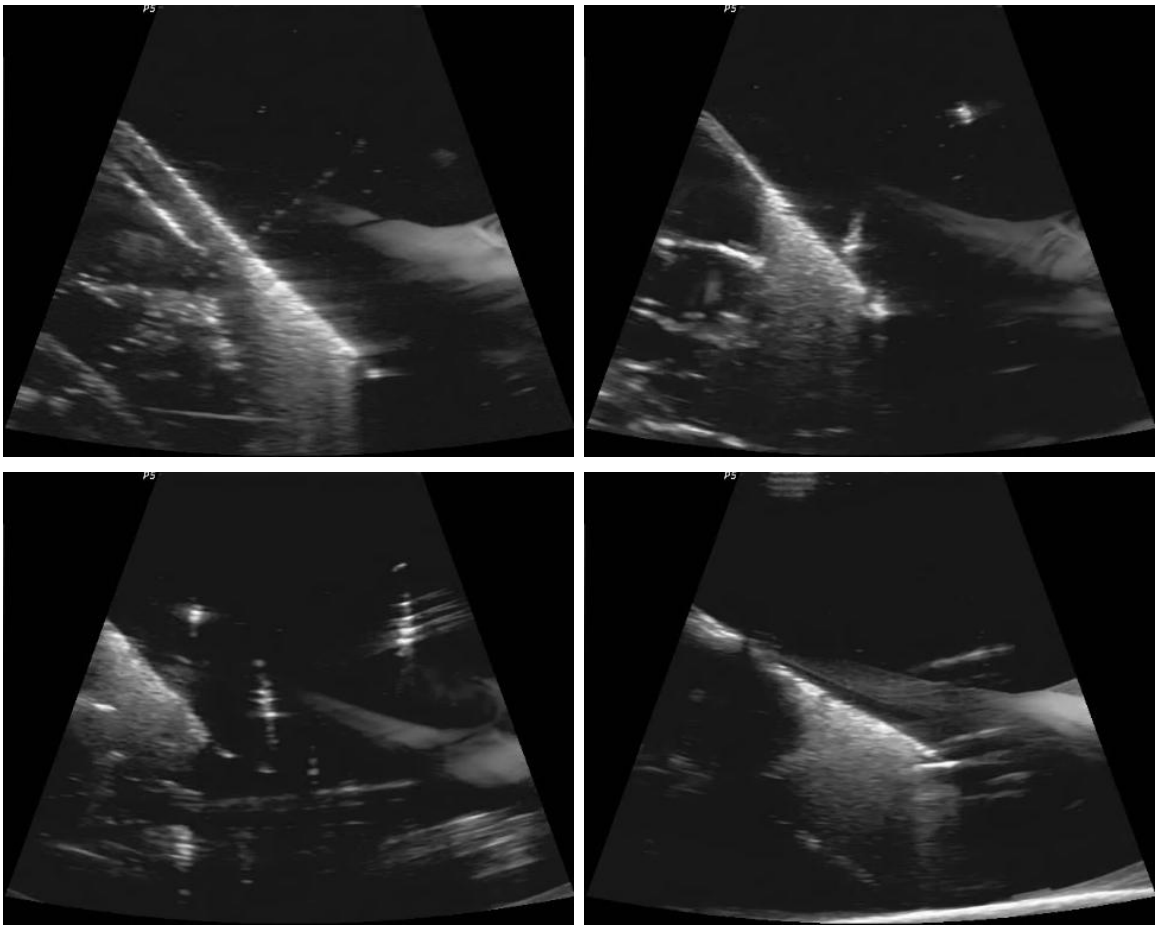

Figure 5: 2D US image of the needle in the gelatine phantom.

3.4 Agar Based Phantom

Agar is one of the most commonly used materials to prepare phantom. Agar based phantoms can realistically mimic tissue in ultrasound imaging. Also, it is easy to prepare it. The speed of sound varies between 1498 and 1600 m/s and attenuation coefficient varies between 0.3 and 2.0 $dB.(cm.MHz)^{-1}$ in the agar based phantoms. Its acoustical properties are in the desired level to mimic human tissue and they can be controlled with additive chemicals. The speed of sound can be controlled with n-propanol concentration and attenuation coefficient can be controlled with graphite concentration. The major property of using n-propanol concentration and graphite is that speed of sound and attenuation change linearly with respect to percentage of

n-propanol and graphite in the mixture, respectively. Hence, the percentages of these chemicals are calculated with linear equations or graphics to obtain desired acoustical properties [42].

The major disadvantages of agar based phantom is that agar based phantoms do not have resistance to microbiological attacks. Agar is a very suitable medium for bacterial growth. Biologists use agar to grow bacteria. Microbiological attack in the phantoms changes the acoustical properties and shorten it durability. In order to preserve phantom and its acoustical properties, preservatives must be used. Hence, its life span can be extended up to 6 months. In our experiments, cholor hexadine has been used as the preservative. It is note that benzalkonium chloride or thimerosal can be used as preservatives.

Soft tissue has been mimicked with agar phantoms in our experiments. Speed of sound and attenuation coefficients are close to 1540 m/s and 0.54 $dB.(cm.MHz)^{-1}$, respectively. In order to prepare 1 lt phantom, following steps are applied. Firstly, the temperature of 860 ml distilled water is raised to 85°C. 30 g agar and 107 ml n-propanol are added. The mixture is heated to 90°C under stirring. It is stirred until its color become transparent. Then, the temperature is cooled under stirring to 46°C and 10 ml cholor hexadine is added. Finally, the mixture poured into polyurethane cap and it is cooled in the refrigerator at least 8 hours. If there are excessive bubbles in the mixture, it can be rested about 15-30 minutes to eliminate them before putting it in the refrigerator. 2D US images of a biopsy needle in the agar phantom prepared with the recipe are shown in figure 6.

3.5 Agar-Gelatine Based Phantom

Agar and gelatin are one of the most frequently used materials to prepare phantom as explained in the previous sections. Attenuation coefficient in agar and speed of sound in gelatin are in the desired level to mimic soft tissue. To realistically mimic

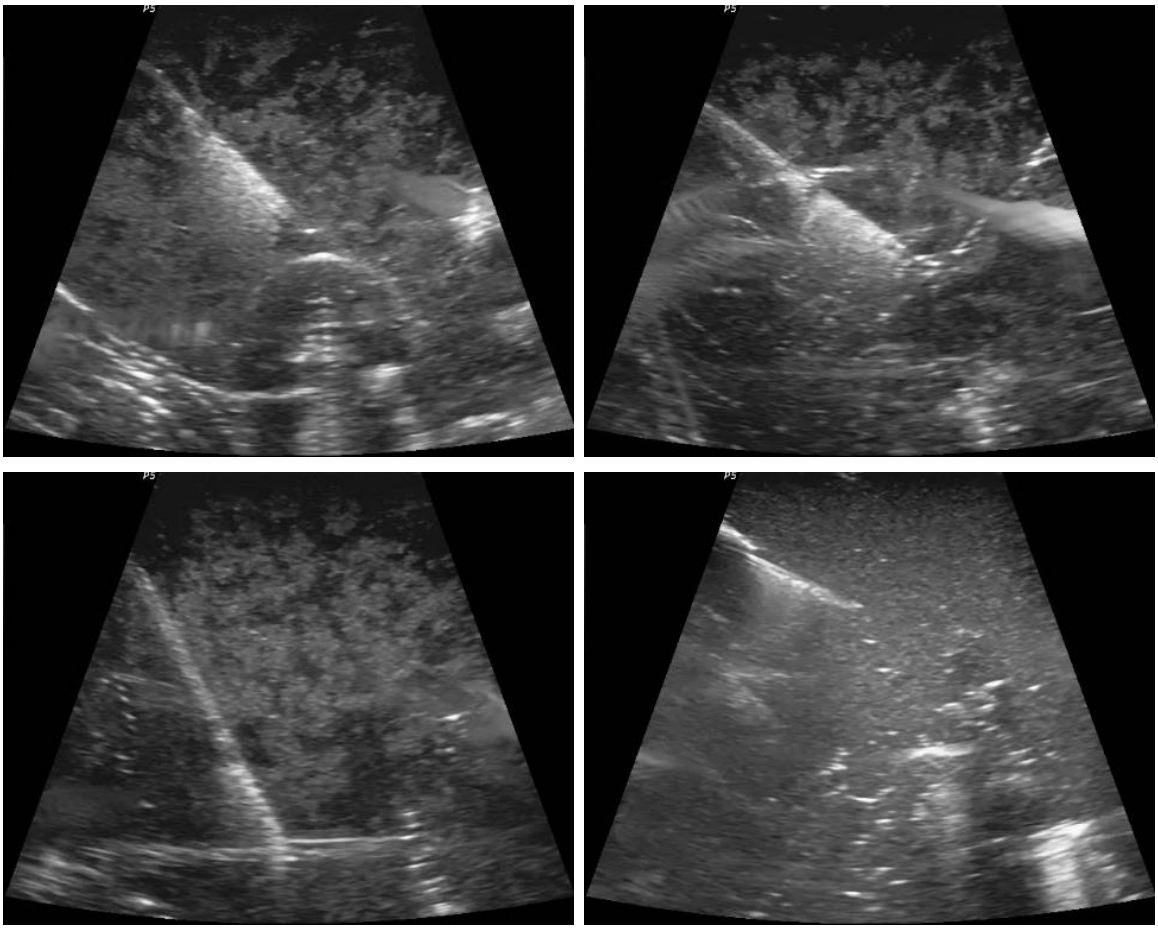

Figure 6: 2D US image of the needle in the agar phantom.

tissue, speed of sound in agar and attenuation coefficient in gelatin are modified with additive chemicals. However, desired acoustical properties can be obtained by mixing agar and gelatin. Also, acoustical properties in the mixture can be controlled with percentages of agar and gelatin [43].

The most important property of this type of phantom is that it can mimic both acoustical and mechanical properties of tissues, especially cancerous and glandular tissues. Mechanical properties can be also controlled with percentages of agar and gelatin (Table 2). It is a very important property because it is not easy to obtain the desired acoustical and mechanical properties at the same time. Hence, agar-gelatin based phantoms are frequently used in applications that acoustical properties are as important as mechanical properties. The most conspicuous examples are needle

insertion with ultrasound guidance and elastography. When the needle is inserted into the tissue, it applies reaction force. Also, needle bends because of lateral forces. Agar-gelatin based phantoms apply tactile feedback and the needle is bent. Hence, the experiments become more realistic. Also, agar-gelatin phantom is important for elastography experiments. Elastography is an imaging technique that maps tissues elastic properties. US images are used to create stiffness map. The main purpose is to determine whether the tissue is hard or soft because cancerous tissue is much harder than healthy tissue. Using elastography cancerous tissue can be determined. Agar-gelatin phantoms provide suitable medium for elastography experiments. Desired mechanical properties can be obtained. Also, it is low cost and easy to prepare.

In our experiments, soft tissue has mimicked. Agar and gelatin percentages in the phantom are 11% and 2%, respectively. Agar and gelatin do not have resistance to microbiological invasions as described in previous sections. In order to preserve the phantom and extend its durability, preservatives must be used. Cholor hexadine, benzalkonium chloride, boric acid or thimerosal can be used to preserve the phantom. In our experiments, benzalkonium chloride has been used to the preserve phantom. In order to prepare 2 lt of phantom, following steps are applied [44]. Firstly, the temperature of 890 ml distilled water is raised to $55°C$ and temperature of the 980 ml distilled water is raised to $80°C$ in separate beakers. Then, 110 g gelatine is added to 890 ml at $55°C$ and 20 g agar is added to 980 ml water at $80°C$. The mixtures are stirred until their colors become transparent. Then, two mixtures are combined and stirred rigorously until its color become transparent. It is cooled until $37°C$ while stirred. It is note that 5 g cellulose powder can be added at $45°C$ to increase attenuation coefficient. Then, 10 ml benzalkonium chloride is added. Finally, the mixture is poured into polyurethane cap and it is cooled in the refrigerator at least for 10 hours. If there are excessive bubbles in the mixture, it can be rested about 15-30 minutes to eliminate them before putting it in the refrigerator. 2D US images

of the biopsy needle in the agar-gelatin phantom prepared with this recipe are shown in figure 7.

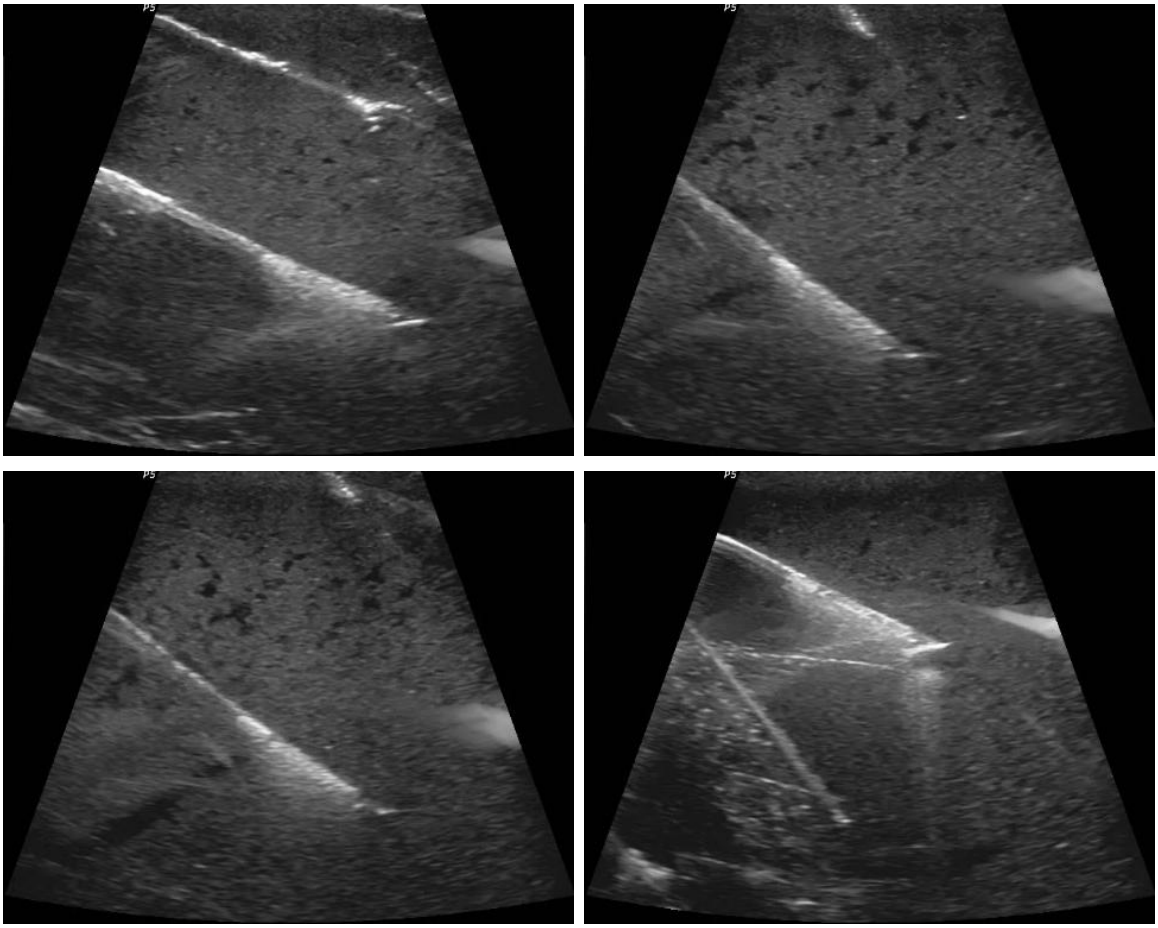

Figure 7: 2D US image of the needle in the agar-gelatine phantom.

Cancerous phantom models also have been prepared in our experiments. The percentages of agar and gelatin in the mixture are 15% and 5%, respectively. The steps above are applied to prepare it. The mixture is poured into spherical molds made from delrin and it is cooled in refrigerator at least 5 hours. Then, the phantom is covered with stretch film. It is embedded into viscous soft tissue phantom about at $30°C$ before putting it in the refrigerator. It is note that stretch film can be replaced with materials made from latex like balloon because it does not affect transmission of sound waves and does not reflect US waves.

Gelatine (%)	Agar (%)	Modulus of Elasticity (KPa)	Human Tissue (KPa)	Mechanic Tissue Type	Acoustic Tissue Type
1	0.5	22 ± 2	19 ± 7	Fat	Fat
2	1	36 ± 2	-	Fat/Glandular	Fat
5	2	33 ± 1	33 ± 1	Glandular	Fat/Glandular
12	4	73 ± 9	-	Cancer	Glandular
15	5	117 ± 8	99 ± 33	Cancer/Fibrous	Cancer

Table 2: Acoustic and mechanical properties of agar-gelatine phantom [45].

3.6 Evaporated Milk Based Phantom

Evaporated milk is another material to produce phantom [46]. The speed of sound and attenuation coefficient in evaporated milk are 1547 m/s and 0.8 $dB.(cm.MHz)^{-1}$, respectively. These acoustical properties are in the desired level to mimic tissues in ultrasound imaging but they should be altered according acoustic properties of desired tissue type. The speed of sound can be controlled with n-propanol concentration and attenuation coefficient can be controlled with distilled water concentration. In our experiments, evaporated milk based phantom has been prepared to mimic human soft tissue. For soft tissue mimicking, the speed of sound and attenuation coefficient in the phantom should be close to 1540 m/s, 0.54 $dB.(cm.MHz)^{-1}$, respectively. In order to

Evaporated milk based phantom can be produced both in liquid and solid forms. Evaporated milk is produced by mixing vigorously 55 g margarine, 400 g sugar, 480 ml skimmed milk and 245 ml boiled water about 5 minutes. Same recipe is used to produce both liquid and solid forms. In order to prepare 1 lt liquid form evaporated based phantom, following steps are applied. Firstly, the evaporated milk is heated until 68°C and it is filtered with vacuum flask. Notice that the temperature of the evaporated milk must not exceed the 72°C because irreversible changes in the evaporated milk occur. Then, 30 ml n-propanol and 370 ml distilled water are mixed in a separate beaker. The mixture and 600 ml evaporated milk are mixed and stirred

gently until its temperature drops to $30°C$. Finally, the mixture is poured into a plastic container.

Solid form evaporated milk based phantom is produced with adding agar. Agar is also used in producing phantom and it alters the acoustical properties of the evaporated milk. Therefore, portions of substitutes are different than portions in liquid form. 1 lt solid form evaporated milk based phantom is produced with applying following steps. Firstly, 644 ml distilled water and 56 ml n-propanol are mixed in a beaker. The mixture is heated until $80°C$ and 28 g agar is added to the mixture. It is stirred until its color become transparent. In the following step, 500 ml evaporated milk is filtered and heated until $55°C$. It is mixed with 500 ml agar solution at this temperature. Finally, the mixture is stirred until its temperature drops to $38°C$. Then, the mixture is poured into a plastic container and it is cooled in the refrigerator at $4°C$ at least 8 hours. The melting point of the solid evaporated milk based phantom is about $80°C$. Therefore, it is thermally stable.

Evaporated milk based phantoms do not have resistance to microbiological attacks. In order to preserve the acoustical properties and extend durability, preservatives must be added to the phantoms. The most powerful preservative is thimerosal for this type of phantom. Thimerosal is an antifungal and antiseptic agent. It is commonly used to extend the self-life of vaccines. It was reported that adding thimerosal (1.33 ml for 800 ml evaporated milk) extents the life of this type of phantom to 2.5 years [46]. Also, the changes in acoustical properties are negligible.

3.7 Polyvinyl Alcohol Based Phantom

Polyvinyl alcohol (PVA) has been proposed as tissue mimicking material to mimic soft tissue [47]. PVA based phantoms are stable and structurally rigid. However, the preparation time of PVA is long and it requires precise temperature control. PVA is synthesized with freezing-thawing method. After the appropriate amount

of PVA is mixed with distilled water, the mixture is freezing 12 hours at $-20°C$. Then, the mixture is thawing 12 hours at $25°C$. The attenuation coefficient of PVA phantom is 0.075 $dB.(cm.MHz)^{-1}$ at the end first freezing-thawing process. The attenuation coefficient can be increased with repeating the process by multiple times. The attenuation coefficient increases to 0.12, 0.21, and 0.22 $dB.(cm.MHz)^{-1}$ in the following cycles. However, the attenuation coefficient is still low to mimic the soft tissue after four freezing-thawing cycles. Therefore, enamel paint is proposed to increase the attenuation coefficient of PVA. For example, if 0.8% enamel paint is added to the PVA-water mixture, attenuation coefficient increases to 0.11 $dB.(cm.MHz)^{-1}$ at the end of the first cycle. If the process is applied multiple times, attenuation coefficient of PVA increases to 0.18, 0.25, and 0.28 $dB.(cm.MHz)^{-1}$ in the following cycles. The speed of sound in PVA varies between 1520 and 1610 m/s. This range is in the desired level to mimic soft tissue. However, the attenuation coefficient in PVA based phantom is low to mimic the human tissue. If the attenuation coefficient can be increased until 0.5 $dB.(cm.MHz)^{-1}$, PVA based phantom can successfully mimic the soft tissue for ultrasound imaging.

3.8 Paraffin Based Phantom

Paraffin has been proposed as a potential substitute to prepare phantom [48]. Paraffin is a very suitable material for mold applications. They are not toxic and have resistance to microbiological attacks. Paraffin based phantoms have the advantage of temperature stability. Their melting point is about $80°C$. Hence, they are durable. Also, it easy to prepare paraffin based phantoms. Attenuation coefficient can be controlled with carnauba wax and micro glass beads. The attenuation coefficient varies between 0.32 and 2.04 $dB.(cm.MHz)^{-1}$. However, it is not easy to control speed of sound in paraffine. The speed of sound is varies between 1425 and 1480 m/s. Compared with human acoustical properties, paraffin can mimic cancerous, abdominal,

and breast tissues in ultrasound imaging. If the speed of sound can be increased with additional substitutes, more realistic mimicking can be obtained.

3.9 Silicon Based Phantom

Silicone products have been proposed as potential substitute to prepare phantom [49]. Silicone is a very suitable material for mold applications. Also, dehydration does not occur and silicone has resistance to microbiological attacks. Thus, silicon based phantoms are stable and durable. However, acoustic properties are not in the desired range to mimic tissue for ultrasound imaging. Speed of sound in the silicone compounds varies between 1059 and 1142 m/s and attenuation coefficient of sound in silicone compounds varies between 0.84 and 1.72 $dB.(cm.MHz)^{-1}$. Compared with acoustic properties of the tissues, the speed of sound in silicone rubber is very low and attenuation coefficient of sound in silicone rubber is very high to mimic the tissues for ultrasound imaging. Hence, silicon oil, glycerol, and vaseline are proposed to adjust the acoustic properties of silicone rubber. However, desired acoustical properties are not obtained with these additional substitutes. For example, attenuation coefficient is adjusted to 0.84 $dB.(cm.MHz)^{-1}$ with adding 40% silicon oil to silicone compound. Another example, speed of sound is increased to 1180 m/s with adding 33% glycerol to the silicone compound but the attenuation coefficient is increased to 1.72 $dB.(cm.MHz)^{-1}$. As seen from these examples, the acoustical properties of silicone are still far from the desired range to mimic the tissues even with additional substitutes. Therefore, silicone rubber compound is not preferable material to mimic the tissues for ultrasound imaging due to the problems in altering acoustical properties.

3.10 Magnesium Silicate Based Phantom

Magnesium silicate is a potential substitute for phantom preparation [50]. Magnesium silicate can mimic the soft tissue with modifying its acoustical properties. The

speed of sound in magnesium silicate is 1458 m/s and attenuation coefficient is 0.04 $dB.(cm.MHz)^{-1}$. Compared with acoustic properties of human tissue, the speed of sound and attenuation coefficient are low. Hence, additional substitutes were proposed to increase speed of sound and attenuation coefficient. In order to increase speed of sound in magnesium silicate, it can be mixed with n-propanol, magnesium, or tetrasodium pyrophosphate. The speed of sound can be increased to 1520 m/s with adding 15% n-propanol, 10% magnesium or 0.4% tetrasodium pyrophosphate. These substitutes increase the speed of sound to the desired level but they do not affect the attenuation coefficient. It can be increased until 0.94 $dB.(cm.MHz)^{-1}$ with graphite or talc. For example, the attenuation coefficient can be increased to 0.52 $dB.(cm.MHz)^{-1}$ with adding 5 gram graphite to 100 gram magnesium silicate. After adding these substitutes, the desired acoustical properties are obtained to mimic soft tissue. Magnesium silicate based phantoms are thermally stable and have resistance to microbiological attacks. However, this type of phantoms are thixotropic (stable form at rest but becoming fluid when agitated) so they are not suitable for mold applications.

CHAPTER IV

NEEDLE LOCALIZATION IN 2D ULTRASOUND IMAGES

This chapter presents a novel image processing method for automated needle localization in 2D US images. The proposed method uses a Gabor filter to segment the needles in US images. The Gabor filtered images are then binarized with an automatic parameter tuning method and the needle trajectory is obtained using line fitting. Finally, location of the needle tip is estimated using the probabilistic mapping method. In this chapter, the completed localization scheme is given in detail, and the effectiveness of the method is shown using different types of tissue phantoms.

There are three commonly used methods for needle detection in US images. The first method is based on the Frangi vesselness filter [19]. The second method is variance mapping [5]. These methods enhance all of the tubular structures in 2D and 3D US images including undesired structures and artifacts. Due to this shortcoming, it is difficult to distinguish needles from other structures (See Fig. 8(c)-(d)). The third method is based on empirical and adaptive thresholding. However, the threshold value can vary from image to image creating discontinuities in the appearance of the needle in the US image (See Fig. 8(e)-(f)) .

Due to these shortcomings of the commonly used methods, we propose a new filtering method based on the Gabor filter to detect biopsy needles in 2D US images [51]. The proposed method consists of four parts: (i) Gabor-based line filtering, (ii) binarization, (iii) axis localization, and (iv) needle tip localization. Steps of the filtering method is shown in Fig. 9. The main difference between the proposed filtering method and others is that this filter enhances the tubular structures in the direction

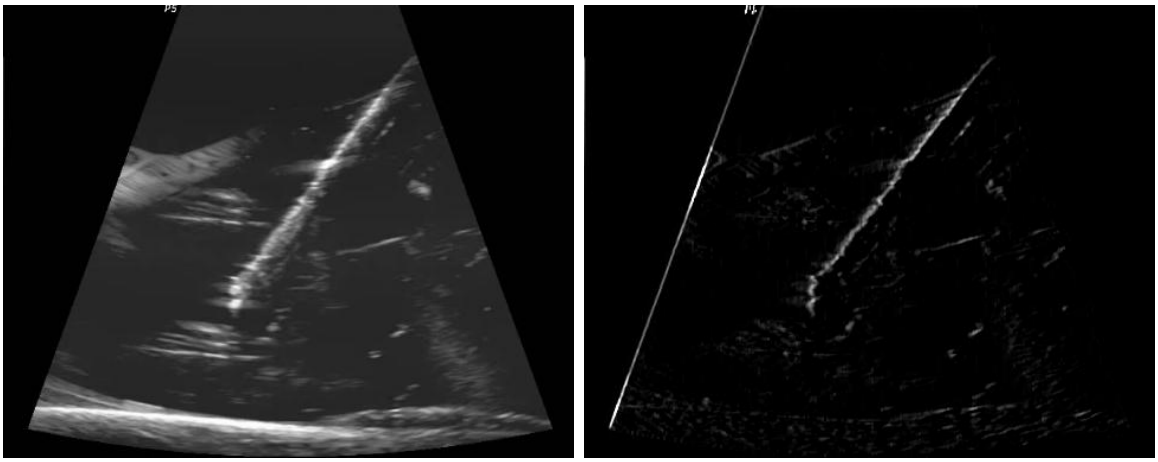

(a) Raw Image

(b) Gabor filter output

(c) Frangi filter output

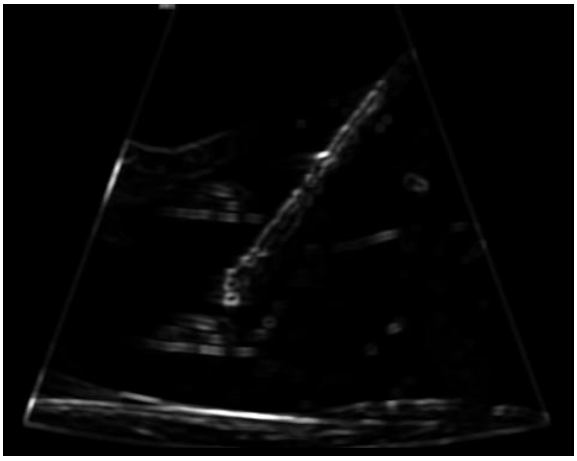

(d) Variance mapping output

(e) Thresholding with T = 128

(f) Thresholding with T = 180

Figure 8: (a) The raw image of the needle in gelatin based phantom. (b) The output of the Gabor filter when the orientation of the filter, θ, equals to 232°. (c) The output of Frangi's vesselness filter when thresholds, α and β, which control the sensitivity of the filter equal to 0.5 and 15, respectively. (d) The output of variance mapping. (e)-(f) The output of simple thresholding for 8-bit US image when the threshold values (T) equal 128 and 180, respectively.

of the needle insertion path, filtering out the orthogonal structures. As a result, the needle pixels become brighter compared to the image background, making the needle stand out. The result of the proposed filtering method is shown in Fig. 8(b). The raw 2D US image in the figure contains artifacts. For instance, the reverberation artifact (at the bottom of the image) can be clearly distinguished. The brightness of this artifact's pixels are higher than the brightness of the needle's pixels. Also, the artifact's shape is very similar to that of a needle. It can be challenging to detect the needles using the previously mentioned methods, because they cannot filter artifacts effectively. But, after the image is filtered using Gabor filtering, the needle pixels become brighter than the most of the artifacts, making the needle distinguishable.

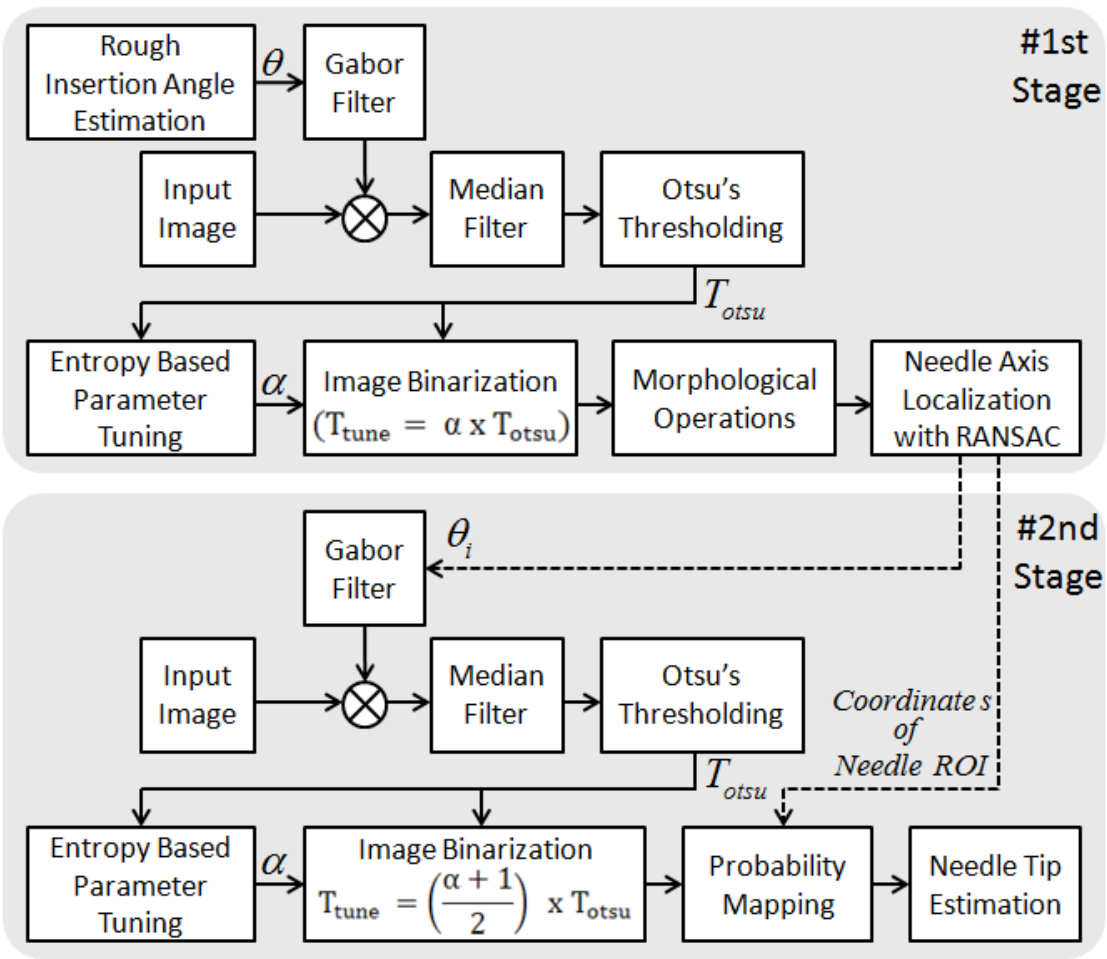

Figure 9: Flowchart of the proposed needle localization algorithm.

4.1 Gabor Filter

Gabor filtering is widely used to identify fingerprint features in the literature [52], and it is also used to detect anatomical structures, such as the liver and retina [53, 54]. The Gabor filter used in this research is adapted from [53].

The 2D Gabor filter function in the spatial domain is the multiplication of a complex carrier sinusoid and a 2D Gaussian envelope:

$$g(x,y) = \exp\left(-\frac{(x')^2+(y')^2}{2\sigma^2}\right)\exp\left(j\left(2\pi\frac{x'}{\lambda}\right)\right) \tag{8}$$

$$\begin{aligned} x' &= x\cos\theta + y\sin\theta \\ y' &= -x\sin\theta + y\cos\theta \\ \lambda &= 0.56\sigma \end{aligned} \tag{9}$$

where σ is the standard deviation value, λ is the wavelength of the modulating sinusoid, and θ is the orientation of the Gabor filter.

$$e^{jx} = cos(x) + jsin(x) \tag{10}$$

Using Euler's formula (10), the 2D Gabor filter can be rewritten as:

$$\begin{aligned} Re\{g(x,y)\} &= \exp(-\frac{(x')^2+(y')^2}{2\sigma^2})\cos(2\pi\frac{x'}{\lambda}) \\ Im\{g(x,y)\} &= \exp(-\frac{(x')^2+(y')^2}{2\sigma^2})\sin(2\pi\frac{x'}{\lambda}) \end{aligned} \tag{11}$$

The line filtered image, $I_g(x,y)$, is the convolution of the input image, $I(x,y)$, and the imaginary part of the Gabor filter kernel, $Im\{g(x,y)\}$, as in (12).

$$I_g(x,y) = I(x,y) * Im\{g(x,y)\} \tag{12}$$

4.2 Estimation of Needle Insertion Angle

The Gabor filter is applied in accordance with an orientation angle, θ. In order to localize the biopsy needle in US images, the orientation of the filter has to be equal to

the insertion angle of the needle because the best appearance of the needle and its tip can be obtained at this angle value. Therefore, this filtering angle is consistent with the needle insertion angle. In Fig. 10, the Gabor filter is applied to the same image by changing the orientation angle in increments of 30°. This image bank shows that the needle visibility is maximized when the filter orientation angle is almost equal to the needle insertion angle, and the artifacts in the image created by other structures are minimized.

The angle estimation is divided into two scenarios based on prior knowledge. When frame sequences are used, prior knowledge is available for the frames; when a single frame is used such data are not available. Two different techniques are proposed below to estimate the needle insertion angles for both scenarios. Needle insertion angle is estimated from a single US image and in frame sequences. In US frame sequences, the information from previous frames can be used to estimate the insertion angle; this information is not available, in single US images. The needle insertion angle is estimated with two different techniques for each case.

4.2.1 Estimation of the Needle Insertion Angle from a single US image

Estimating insertion angle value in an image is quite complicated unless the angle is known a priori. A method based on the quadrants of cartesian coordinate system was developed to estimate the needle insertion angle in 2D US images. With this method, a rough estimate of the insertion angle, α, is chosen first as shown in Fig. 11(b). If the needle trajectory is similar to the trajectories as shown in quadrants I and III, we choose the initial insertion angle, α, to be 135°, and for the quadrants II and IV, we choose α to be 225°. After the initial assignment, the Gabor filter is applied using the estimated insertion angle. The needle trajectory becomes clearer and the RANSAC line estimator is applied, where the slope of the line, m, is found. The exact insertion angle in terms of the Gabor filter coordinate system, θ, can be found more precisely

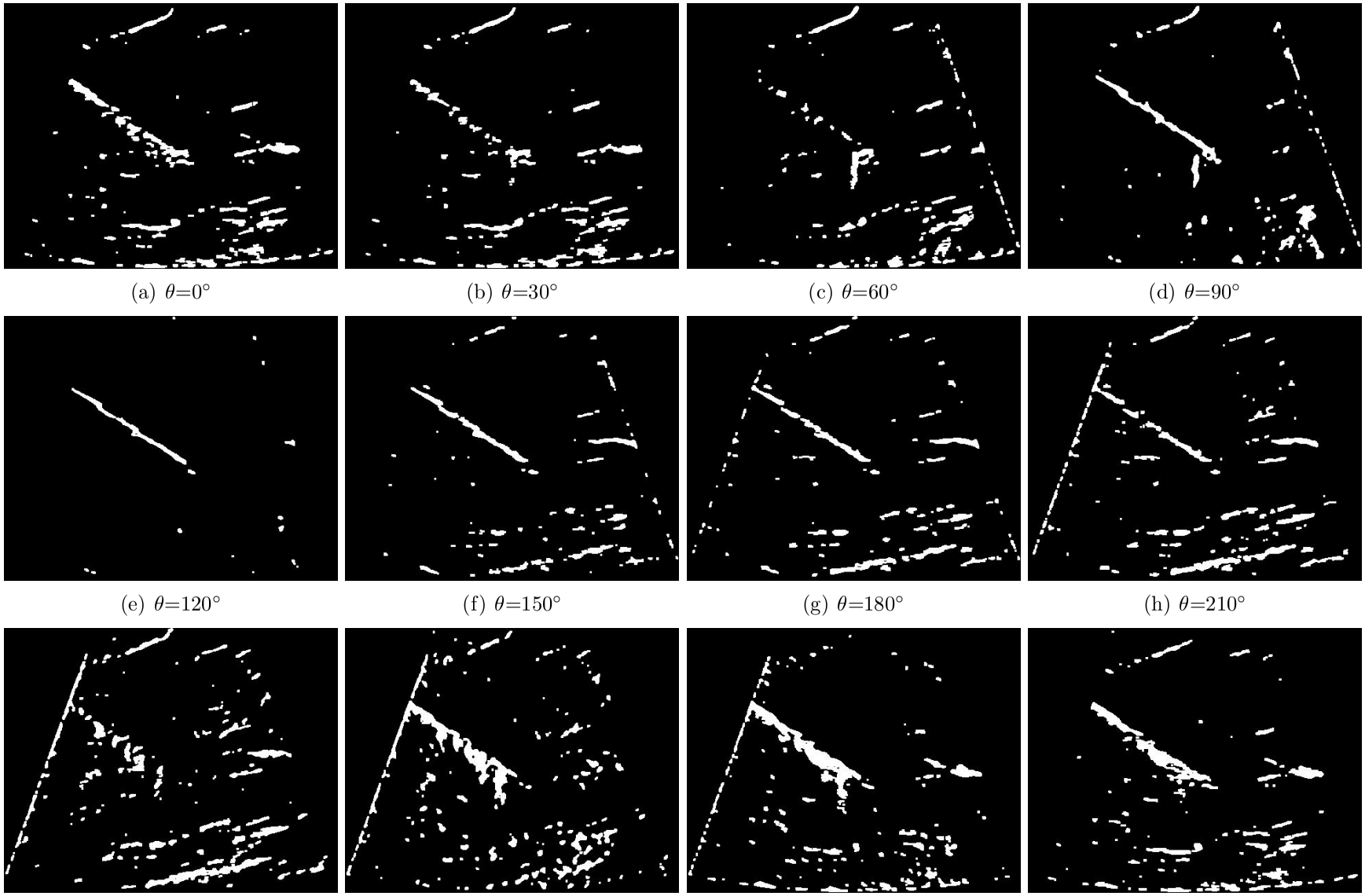

(a) θ=0° (b) θ=30° (c) θ=60° (d) θ=90°

(e) θ=120° (f) θ=150° (g) θ=180° (h) θ=210°

(i) θ=240° (j) θ=270° (k) θ=300° (l) θ=330°

Figure 10: The output of the Gabor filter bank using the proposed line filter. The orientation angle, θ, is changed in 30° increments to show the filtering effects.

at this point and then it can be used in the Gabor filter again to localize the biopsy needle.

Due to the way the US images are collected, the coordinate frames of the needle axis and the Gabor filter are not similarly aligned, as shown in Fig. 11(a). Using (13), the exact insertion angle value is expressed in terms of the Gabor filter coordinate system.

$$\theta = \alpha + \mid \tan^{-1}(m) \mid -45^{\circ} \tag{13}$$

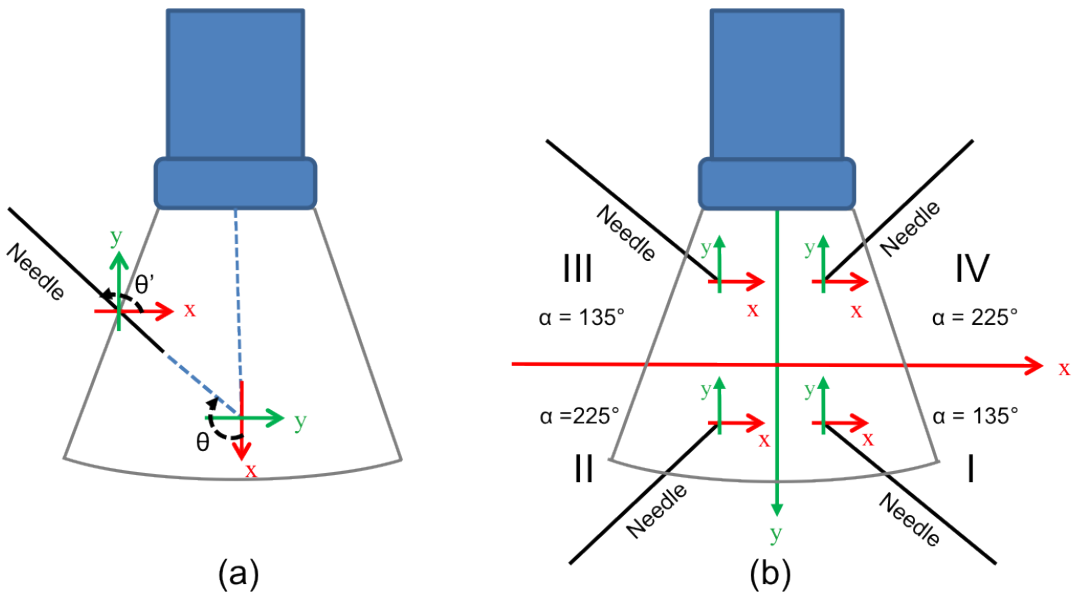

Figure 11: The US and needle coordinate systems. (a) Angle θ. (b) Possible α angles for the quadrants.

Steps of the needle insertion angle estimation is depicted in Fig. 12 for two different types of gel phantoms. First, raw images are collected ((a) and (f)). Second, a rough estimate of the insertion angle is chosen and the Gabor filter is applied ((b) and (g)). Next, the RANSAC line estimator is applied to get the exact insertion angle, θ ((c) and (h)). Finally, the Gabor and the RANSAC are repeated to localize the needle and its tip ((d-e) and (i-j)).

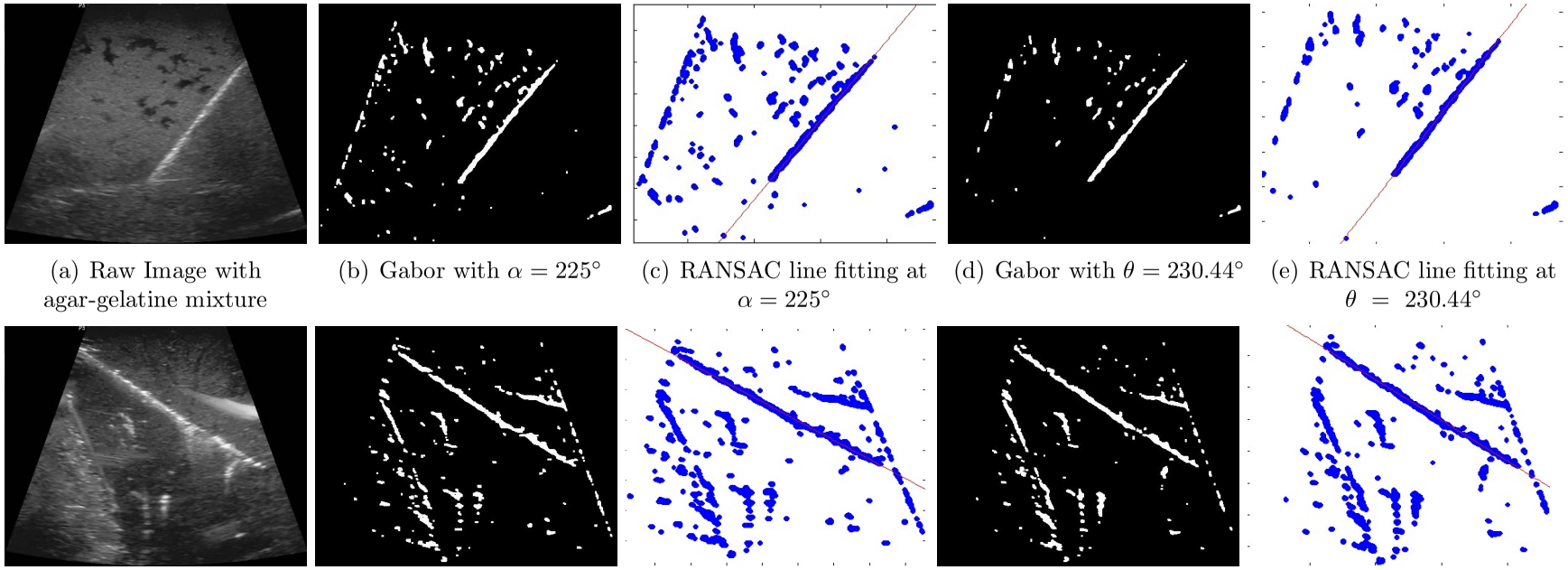

(a) Raw Image with agar-gelatine mixture (b) Gabor with $\alpha = 225°$ (c) RANSAC line fitting at $\alpha = 225°$ (d) Gabor with $\theta = 230.44°$ (e) RANSAC line fitting at $\theta = 230.44°$

(f) Raw Image with agar (g) Gabor with $\alpha = 135°$ (h) RANSAC line fitting at $\alpha = 135°$ (i) Gabor with $\theta = 122.43°$ (j) RANSAC line fitting at $\theta = 122.43°$

Figure 12: The order of the needle insertion angle estimation and detection in 2D US images. (a) The raw image of the needle in agar-gelatin based phantom. (b) Gabor filter applied with estimated insertion angle $\alpha = 225°$. (c) RANSAC line fitting to determine needle axis. (d) Gabor filter applied at exact insertion angle $\theta = 230.44°$. (e) RANSAC line fitting to localize the needle and its tip. (f) The raw image of the needle in agar based phantom. (g) Gabor filter applied using estimated insertion angle $\alpha = 135°$. (h) RANSAC line fitting to determine the needle axis. (i) Gabor filter applied using exact insertion angle $\theta = 122.43°$. (j) RANSAC line fitting to localize the needle and its tip.

4.2.2 Estimation of the Needle Insertion Angle in Frame Sequences

In US image sequences (i.e., videos), the needle insertion angle can be determined at the beginning of the needle penetration and can be assumed constant afterwards. Therefore, the needle insertion angle, θ, is determined before the filtering is applied. The differences in close frames can be used to estimate the insertion angle. In general, the image acquisition speed of the US devices are 30 frames per second (fps). Two images that are one second apart can be used for angle estimation assuming that the displacement of the US probe is zero at the beginning of the needle insertion and the tissue (i.e., phantom) does not move, as shown in (14).

$$I_n = I[kn] - I[k(n-1)] \tag{14}$$

where I is the input image, I_n is the difference image, k is the frame step, and n = 1,2,3,... is the frame number. This process generates a bank of binary images. The needle insertion angle is updated as data are collected. Initially, we used the least square method is used to detect the insertion angle by fitting a line to the needle pixels. However, due to the artifacts in the image differences, the error in the angle estimation increased dramatically. We observed that the needle pixels obtained from the frame difference images lie in the maximum variance region. Therefore, the principal component analysis was used to get the best insertion angle. Then, covariance matrix of PCA was calculated as:

$$\Sigma = \begin{bmatrix} \sigma_{xx}^2 & \sigma_{xy}^2 \\ \sigma_{yx}^2 & \sigma_{yy}^2 \end{bmatrix} \tag{15}$$

where

$$\sigma_{xy}^2 = \frac{\sum_{i=1}^{N}(x_i - \bar{x})(y_i - \bar{y})}{N} \tag{16}$$

and x_i and y_i are the coordinates of the white pixels in the binary image, $\bar{x}$ and $\bar{y}$ are the means of x_i and y_i, respectively, and N is the number of the white pixels in the

sum of the difference images. Then, the corresponding eigenvector υ in this direction is:

$$\upsilon = \begin{bmatrix} \upsilon_{(1,1)} & \upsilon_{(1,2)} \\ \upsilon_{(2,1)} & \upsilon_{(2,2)} \end{bmatrix} \tag{17}$$

The angle of major principal axis, θ_m, in this direction is:

$$\theta_m = \left(-\tan^{-1}\left(-\frac{\upsilon_{(2,1)}}{\upsilon_{(1,1)}} \right) \right) \tag{18}$$

The needle insertion angle equals to the sum of the major principal axis in this direction and π. Since the result of $\tan^{-1} \in [-\pi, \pi]$, π is added to θ_m for the Gabor filter to work:

$$\theta = \theta_m + \pi. \tag{19}$$

Steps of the needle insertion angle estimation for frame sequences is shown in Fig. 13. Two images that are 30 frames apart in a sequence are chosen. These images are binarized and their difference is obtained (Fig. 13(c)). Then, to detect the needle insertion angle, the Gabor filter followed by RANSAC line fitting is applied (Fig. 13(d-e)).

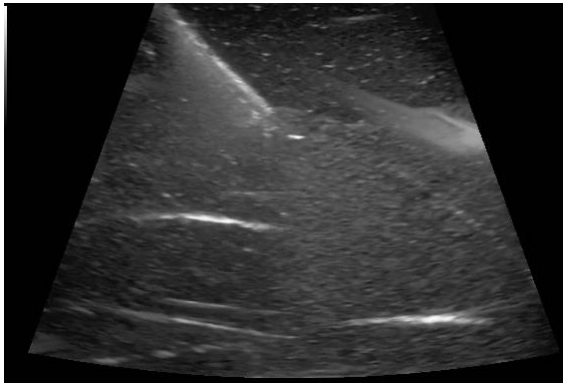

(a) Frame #96

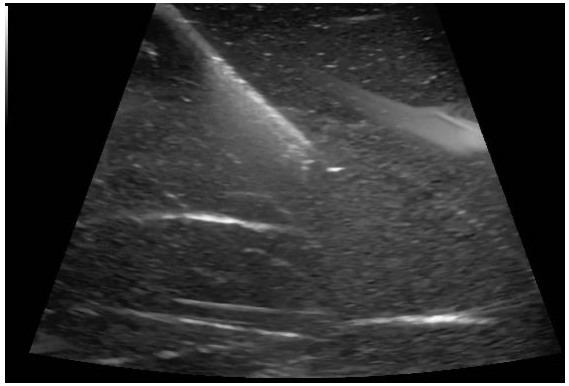

(b) Frame #126

(c) Frame Difference Image

(d) Gabor with $\theta = 135.34°$

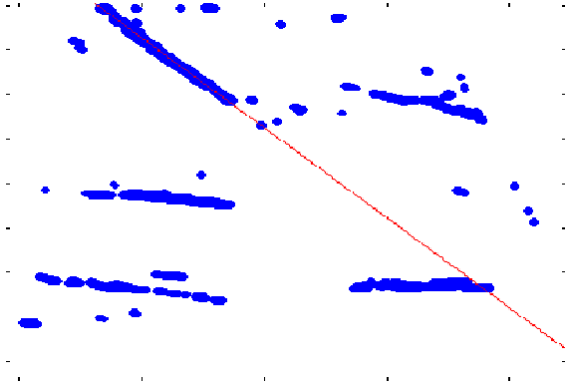

(e) RANSAC Line Fitting

Figure 13: The order of the needle insertion angle estimation and detection in 2D US frame sequences. (a) and (b) are raw images of the needle in agar-based phantom. (c) The difference image after the binarization process. Smoothing, thresholding, and morphologic operations are applied respectively. (d) Gabor filter applied using the estimated insertion angle, $\theta = 135.34°$. (e) RANSAC line fitting to localize the needle.

4.3 NEEDLE AXIS LOCALIZATION

4.3.1 Image Binarization

After the Gabor-based line filtering, image binarization is required for line fitting. Binarization is achieved in three steps: smoothing, thresholding, and removing small particles. The steps are explained in detail below.

4.3.1.1 Median Filtering

After the Gabor-based line filtering is applied, the output image contains considerable noise (Fig. 8(b)), and the image should be smoothened for thresholding operations. Therefore, a median filter is used to smoothen the image and reduce noise. A 7×7 sized kernel was used for images and frame sequences. This median filter enhances the needle edges. The output of the median filter is shown in Fig. 14(c).

4.3.1.2 Automatic Thresholding

Thresholding is required to get an outline of the needle but we observed that the threshold value is not constant after the median filter is applied. Therefore, an automatic thresholding method was needed. To determine the threshold value, Otsu's thresholding method [55] was used. For the difference image of close frames, the automated thresholding value was used directly. However, the threshold value obtained by Otsu's method can binarize an excessive number of pixels as the foreground of single images because of low intensity levels of the needle pixels and the artifacts. At this point, the RANSAC algorithm can fail. To prevent this and increase the success rate of the method, Otsu's threshold value was multiplied with a tuned constant which was selected between 2 and 4. However, this tuned constant changes according to the image medium. In order to calculate this parameter automatically, an entropy based parameter tuning method for Otsu's thresholding is proposed. It is described in Section 4.3.3.

4.3.1.3 Morphologic Operations

After automatic thresholding operations, a 3×3 square shaped structuring element morphologic erosion and dilation is applied. After thresholding, the noise is reduced using morphologic erosion. Even though morphologic erosion reduces the noise, it deteriorates the continuity of the needle. Therefore, morphologic dilation is applied in order to enhance the needle structure, and improve the needle continuity. The result of the morphologic operations is shown in the most right column of Fig. 14(e).

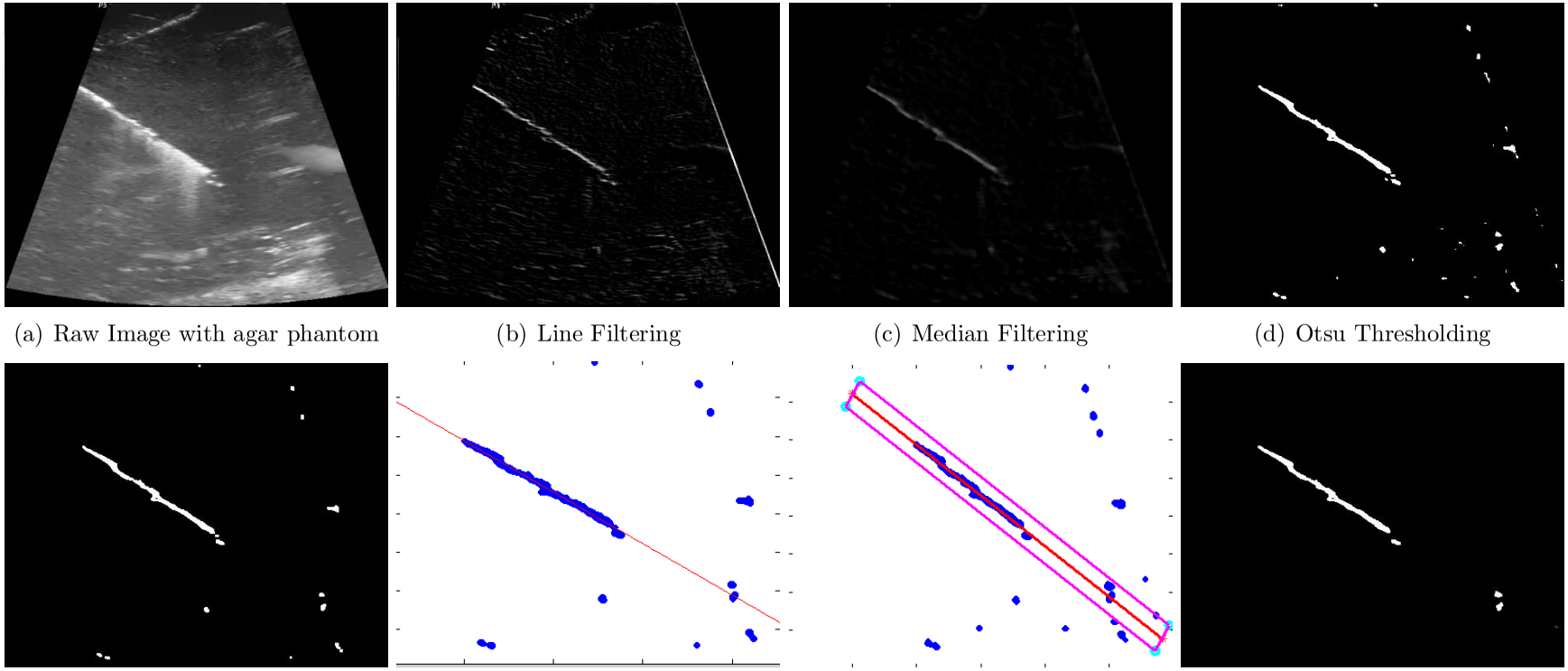

(a) Raw Image with agar phantom (b) Line Filtering (c) Median Filtering (d) Otsu Thresholding

(e) Morphological Operations (f) Axis Localization (g) Axis Localization and ROI (h) Cropped image

Figure 14: (a) Raw image acquired from agar-based phantom, (b) Gabor filter based line filtering when θ=119°, (c) median filtering, (d) thresholding with Otsu's method, (e) morphological erosion and dilation, (f) axis localization using RANSAC, (g) region of interest (ROI) when $N = 6$, and (h) Binarized ROI image.

4.3.2 Line Detection & Region of Interest

In the binarization step, the needle pixels can be classified as background. In this case, the needle cannot be a complete line structure in the images and there can be gaps between the needle pixels. Hence, the needle is detected using a RANSAC algorithm which is a robust line estimator. Briefly, RANSAC algorithm starts by randomly selecting points from a point cloud and a line is fitted onto the selected points. Then, model parameters are calculated and the consistency of the parameters are evaluated. The same process is applied to the remaining points in the point cloud for a best fit. Although the line is discontinuous in the binarized image, the RANSAC can effectively distinguish the line outline.

After the needle trajectory was found, a region of interest (ROI) was selected around the needle pixels to increase the effectiveness of the needle tip detection. This also decreased the computation time. The coordinates of the ROI was calculated as:

$$\begin{aligned}
width &= x_2 - x_1 \\
height &= y_2 - y_1 \\
length &= \sqrt{width^2 + height^2} \\
(x_s, y_s) &= \left(\frac{N \times height}{2 \times length}, \frac{N \times width}{2 \times length}\right) \\
(x_f, y_f) &= (x_1 - x_s, y_1 + y_s) \\
(x_{sec}, y_{sec}) &= (x_1 + x_s, y_1 - y_s) \\
(x_{th}, y_{th}) &= (x_2 + x_s, y_2 - y_s) \\
(x_{ft}, y_{ft}) &= (x_2 - x_s, y_2 + y_s)
\end{aligned} \tag{20}$$

where (x_1, y_1), (x_2, y_2) are coordinates of the needle trajectory obtained by the

RANSAC; (x_s, y_s) are translation distances according to the original coordinate position; (x_f, y_f), (x_{sec}, y_{sec}), (x_{th}, y_{th}), and (x_{ft}, y_{ft}) are the coordinates of the rectangular ROI; N is the thickness of the ROI in terms of pixels. These coordinates are depicted in Fig. 15.

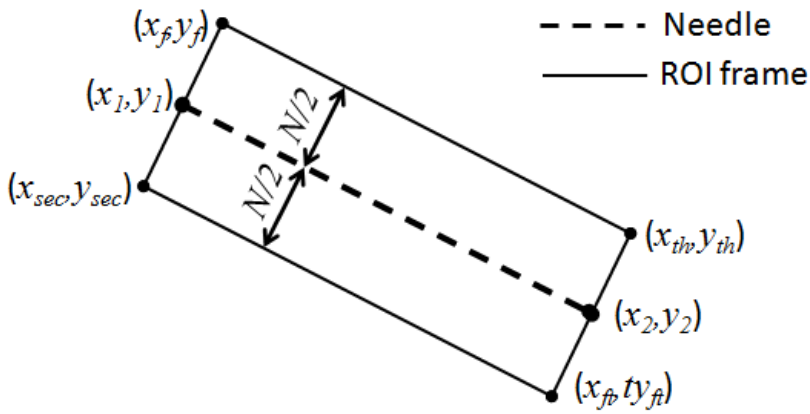

Figure 15: Needle region of interest coordinates.

4.3.3 Parameter Tuning for Otsu's Thresholding

Generally, US images contain noise and artifacts. Therefore, the intensity level of the needle pixels can be very close to the image background's. If the image is not binarized with a proper threshold value, the needle pixels can be classified as background or an excessive number of artifacts can be classified as foreground. In this case, the RANSAC algorithm can fail.

A constant value was selected as Otsu's threshold parameter according to the image background intensity in [2]. However, this parameter varies by image. Although this parameter can be selected according to the specific image medium that is used, an optimal value is hard to obtain. A tuned threshold value was acquired by multiplying Otsu's threshold with a pre-tuned constant, α, in [2] and [21] to improve the success rate of the method. Below, an entropy based automatic α parameter tuning method is explained to find an optimal threshold value for Otsu's method.

Entropy based automatic parameter tuning is based on four image features: (i)

foreground entropy, (ii) background entropy, (iii) ratio of the number of white pixels (obtained from the original Otsu threshold value, (T_{otsu}), to the total number of pixels in the image, and (iv) entropy of the Gabor filtered image. The entropy values are calculated according to the method given in [56] and [57].

Entropy (H), foreground entropy (H_f), and background entropy (H_b) are calculated as:

$$H = -\sum_{i=0}^{L-1} p(i) \log_2 p(i) \tag{21}$$

$$H_b(T_{otsu}) = -\sum_{i=0}^{T_{otsu}} \frac{p(i)}{P_b(T_{otsu})} \ln\left(\frac{p(i)}{P_b(T_{otsu})}\right) \tag{22}$$

$$H_f(T_{otsu}) = -\sum_{i=T_{otsu}+1}^{L-1} \frac{p(i)}{P_f(T_{otsu})} \ln\left(\frac{p(i)}{P_f(T_{otsu})}\right) \tag{23}$$

where

$$p(i) = \frac{h(i)}{N}, \text{ i = 0,1,2,. . . , L-1,}$$

$$P_b(T_{otsu}) = \sum_{i=0}^{T} p(i), \;\; P_f(T_{otsu}) = \sum_{i=T+1}^{L-1} p(i),$$

where $p(i)$ is the probability mass function of the image, N is the total number of the pixels in the image, i is the intensity level, $h(i)$ is the total number of the pixels where the intensity level equals to i, and L is the possible maximum number of the pixel levels. The acquired images have 8 bit grayscale resolution, therefore $L = 2^8$ was used.

The entropy based parameter tuning method was developed to perform both in homogenous and heterogenous image backgrounds. According to our experiments, the tuning parameter, α, is very close to the entropy value, H, of images with heterogenous backgrounds. On the other hand, for images with homogenous backgrounds, the parameter value is close to the summation of the image entropy, H, and the ratio

of the background entropy to the foreground entropy, H_b/H_f. In heterogenous backgrounds, the background entropy to the foreground entropy ratio is high. A third parameter should be added to the entropy summation to tune the parameter for both types of image backgrounds. This parameter should not affect the entropy summation for homogenous images but should reduce the entropy summation for heterogenous images. This parameter should also distinguish the background composition. This could be achieved by using the ratio of the total number of foreground pixels (obtained from Otsu's threshold method) to the number of total pixels, W_{ratio}, given in (24).

$$W_{ratio} = \frac{\sum_{i=0}^{h} \sum_{j=0}^{w} (I(i,j) \geq T_{otsu})}{N} \tag{24}$$

If the W_{ratio} is subtracted from the entropy summation, optimal α parameter would be achieved. Then, the parameter to be multiplied with Otsu's threshold is defined as:

$$\alpha = H + \frac{H_b}{H_f} - W_{ratio}. \tag{25}$$

The optimum threshold (T_{tuned}) is calculated as:

$$T_{tuned} = \alpha \cdot T_{otsu}. \tag{26}$$

After parameter tuning operations, line-shaped structuring elements were applied for morphological erosion, and 3×3 square shaped structuring elements were applied for morphological dilation.

The proposed automated parameter tuning method can work with different types of image backgrounds as shown in Fig. 16. Although the excessive number of pixels were determined as the foreground, the optimal threshold values were obtained thanks to the proposed parameter tuning method. The expected outcome of this tuning method is to reduce the processing time during the RANSAC line fitting and to

eliminate the failures which result from the excessive number of foreground pixels that are due to pre-tuned Otsu method.

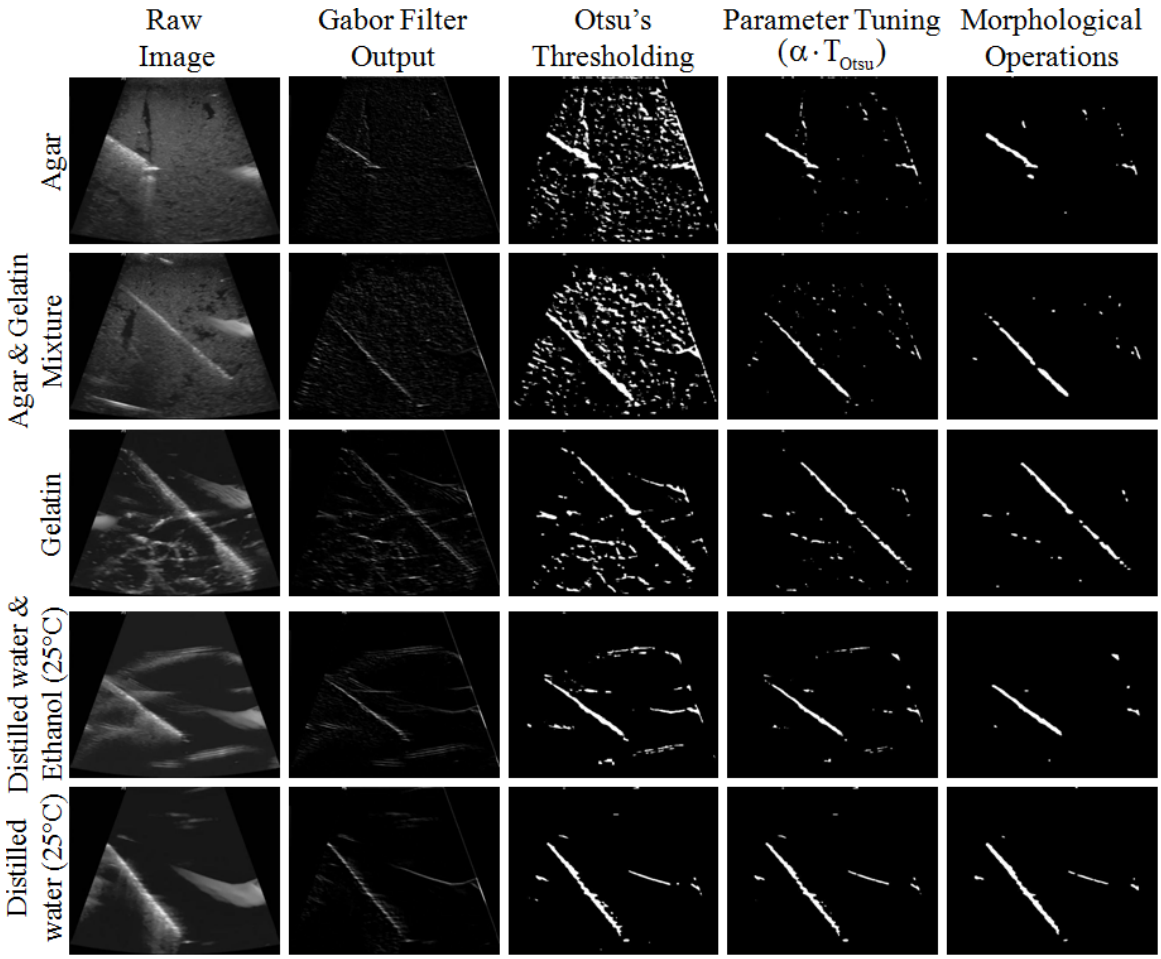

Figure 16: Results of the proposed entropy-based parameter tuning method. Each row represents results from a different phantom. Columns are output images of the proposed method's consecutive steps.

4.4 Location Estimation of the Needle Tip

Finding the exact location of the needle tip is a difficult task, because the visibility of the needle tip changes with the needle's position. In cases where the needle is orthogonally imaged, the needle's position and the orientation determines how the needle and its tip are seen. The needle can be imaged as a complete structure if the bevel of the tip is facing away from the US probe. However, the needle tip might be

seen as a small circular-shaped independent structure at the end of the needle, if the bevel tip is facing towards the probe [58].

If the US image is noisy or the needle is close to other structures, the needle tip cannot be differentiated as a bounded or an unbounded structure. Therefore, the position of the needle tip cannot be recognized in US images, unless an external sensor is used. However, the needle tip can also be estimated from the images.

Here, a probability map based needle tip estimation algorithm is proposed in order to estimate the needle tip position in 2D US images (Fig. 9). In the first part of this needle tip detection algorithm, the input image is convolved using a Gabor filter kernel created using the exact insertion angle (θ_i) of the needle. Then, the visibility of the needle structure, especially its tip, reaches to a maximum in the convolved image; while, the background's and the artifacts' intensity levels decrease to a minimum. Next, a 7×7 sized kernel Median Filter is applied to reduce the noise in the Gabor filtered image.

In the binarization step, the image is binarized using the mean of the Otsu's threshold value and the tuned threshold value. Then, the Otsu's threshold classifies an excessive number of pixels as the foreground (as seen in Fig. 19-(d)). The entropy based parameter tuning segments the minimum number of foreground pixels to be used for RANSAC line fitting. In this algorithm, the continuity of the needle is lost when only the tuned threshold value is used. Therefore, the optimum threshold value is obtained by averaging the two threshold values.

In order to estimate the needle tip, a probability map is created. This map shows the probability of each pixel belonging to the needle tip in the region of interest (ROI). The probability map changes based on the geometrical model of the needle, the binarized US image, and the output of the Gabor filter.

According to the basic mechanics of the materials, the needle curvature can be estimated by a third order polynomial in the US images. In our tests with phantoms,

the needle's geometrical shape was very close to a straight line (the coefficient of the cubic term was 10^{-4} in our hardest phantom gel). Therefore, the needle ROI is selected as a rotated rectangle. Then the ROI is scanned line by line, and for each point on the line the number of white and black pixels both before and after the point, are counted. The white pixels up until the threshold point are assumed to be the detected needle pixels, and black pixels are assumed to be the undetermined needle pixels. The white pixels beyond the threshold point are assumed to be non-needle pixels that are determined incorrectly, and the black pixels are assumed to be non-needle pixels. The probability of each point on the needle is calculated using conditional probability using these measurements. In short, the probability of belonging to the needle is calculated for only selected points on the line. The probability of a point being a true needle pixel, ($P(N \mid +, n_{xy})$), is calculated as:

$$\begin{aligned} P_1 &= \frac{whites\ until\ needle}{(whites\ until\ needle + blacks\ until\ needle)} \\ P_2 &= \frac{blacks\ until\ needle}{(whites\ until\ needle + blacks\ until\ needle)} \\ P_3 &= \frac{whites\ after\ needle}{(whites\ after\ needle + blacks\ after\ needle)} \\ P_4 &= \frac{blacks\ after\ needle}{(whites\ after\ needle + blacks\ after\ needle)} \end{aligned} \tag{27}$$

$$P(N, n_{x,y}) = (P_1 + P_3)P_1 + (P_2 + P_4)P_4 \tag{28}$$

$$P(+ \mid N, n_{x,y}) = P_1 \tag{29}$$

$$P(+, n_{x,y}) = (P_1 + P_3)P_1 + (P_2 + P_4)P_2 \tag{30}$$

$$P(N \mid +, n_{xy}) = \frac{P(N, n_{x,y})P(+ \mid N, n_{x,y})}{P(+, n_{x,y})} \tag{31}$$

It is important that, this probability is combined with the Gabor filter output, because Otsu's threshold method can binarize an excessive number of non-needle pixels. These non-needle pixels can also yield high probabilities, which would mark

these pixels as needle tip pixels. However, if the input image is filtered using a Gabor filter kernel, the visibility of the needle structure, especially its tip reaches to a maximum. By multiplying the probability value with the absolute intensity level of the Gabor filter output, as in (32), false needle tip estimations can be eliminated.

$$P(T \mid +, n_{xy}) = P(N \mid +, n_{xy}) \cdot \mid I_g(n_{x,y}) \mid \tag{32}$$

Sample needle probability maps that are obtained from a needle inserted into different phantoms are shown in Fig. 17 and Fig 18. As a final step, the probability of each pixel is calculated and the location which has the maximum probability is estimated as the needle tip location ($Tip_{(x,y)}$):

$$Tip_{(x,y)} = \arg\max_{n_{x,y}} P(T \mid +) \tag{33}$$

The steps of the proposed needle tip estimation method are shown in Fig. 19. A needle probability map that is obtained from a needle inserted into an agar phantom (see Fig. 19-a) is shown in Fig. 20. Notice that probability reaches its highest value at the needle tip.

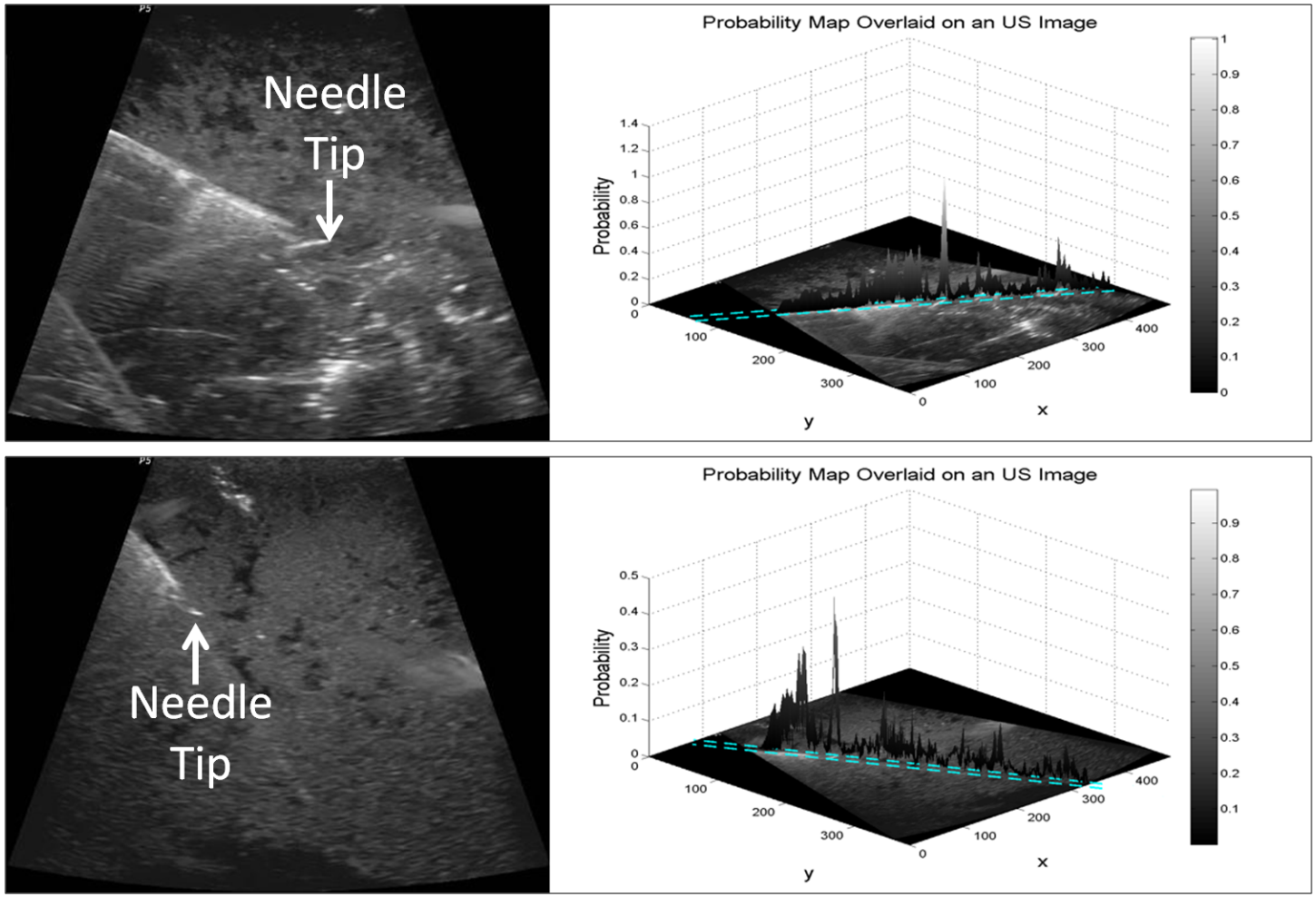

Figure 17: Three dimensional probability map of the needle's tip overlaid on the 2D US images of the agar and agar-gelatin based phantoms, respectively.

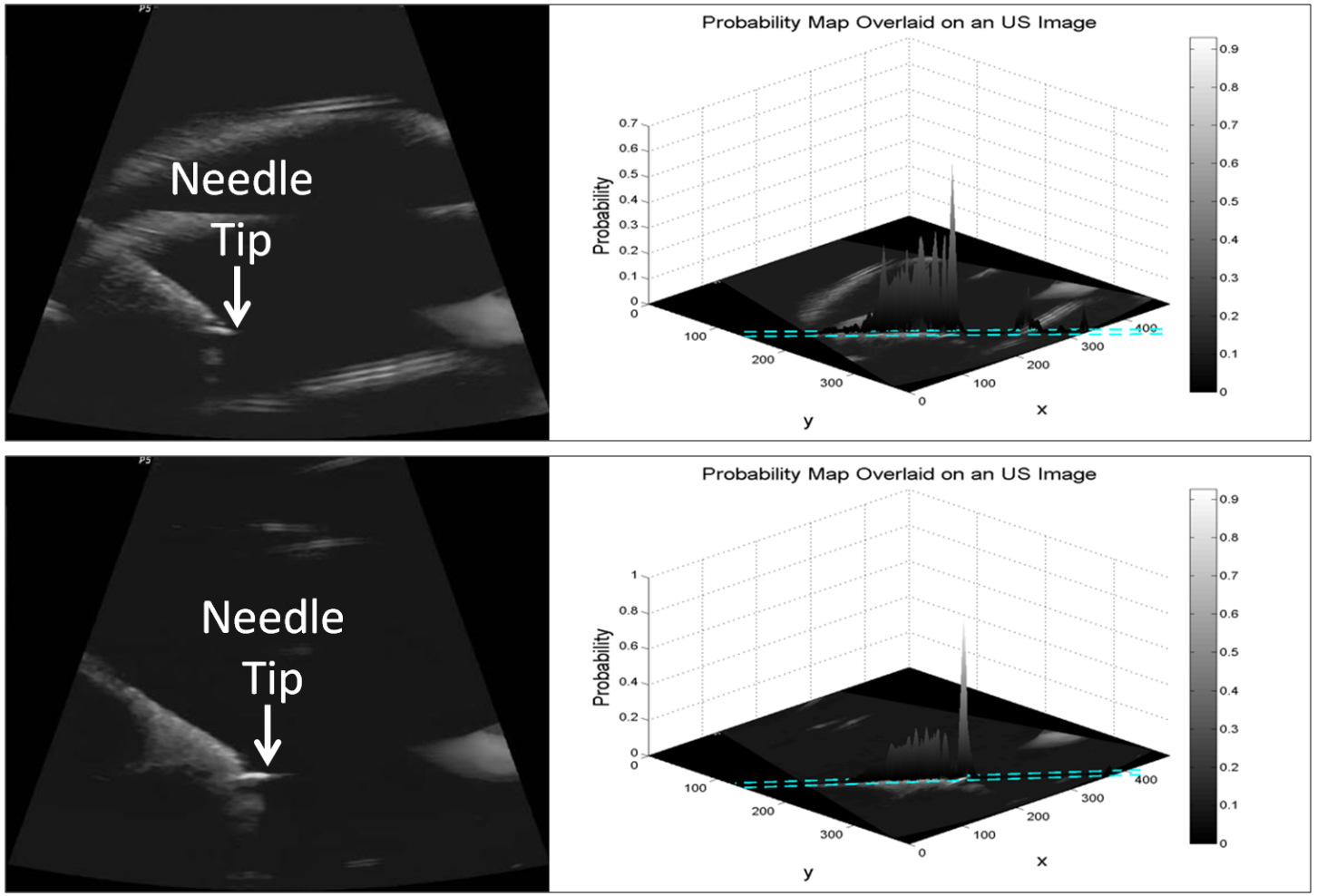

Figure 18: Three dimensional probability map of the needle's tip overlaid on the 2D US images of the water-ethanol phantom and water medium, respectively.

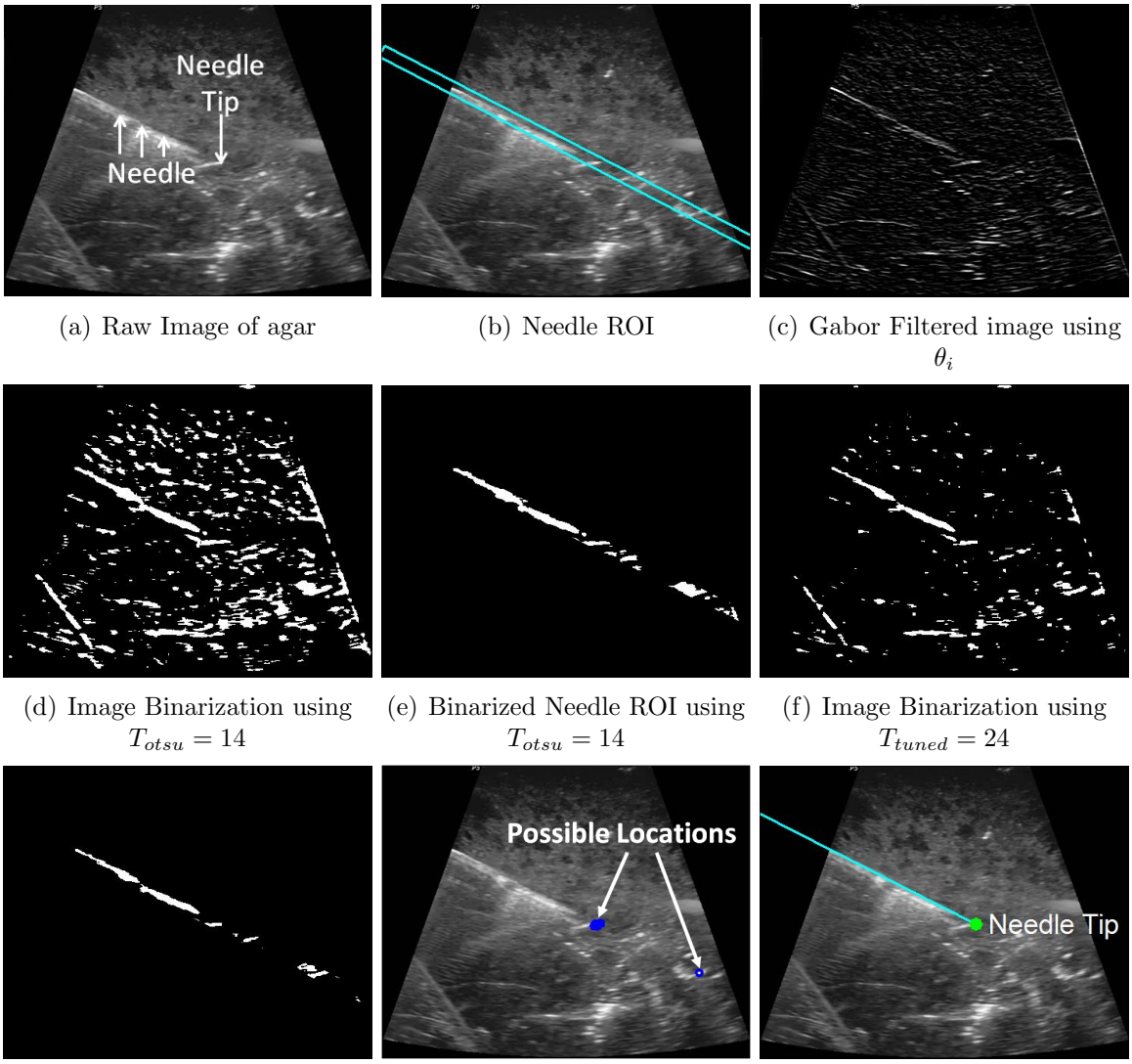

(a) Raw Image of agar

(b) Needle ROI

(c) Gabor Filtered image using θ_i

(d) Image Binarization using $T_{otsu} = 14$

(e) Binarized Needle ROI using $T_{otsu} = 14$

(f) Image Binarization using $T_{tuned} = 24$

(g) Binarized Needle ROI using $T_{tuned} = 24$

(h) Possible needle tip locations

(i) Estimated needle tip location

Figure 19: **(a)** 8-bit raw image of the agar based phantom. **(b-c)** The needle ROI and its insertion angle $\theta_i = 152.71°$ were determined with the Gabor-based needle localization algorithm with the reference angle $\theta = 135°$. **(d)** Thresholding with Otsu's method. **(e)** Binarized needle ROI of (d). **(f)** Thresholding with the mean of Otsu's threshold and the tuned threshold. **(g)** Binarized needle ROI of (f). **(h)** Possible needle tip locations. **(i)** Estimated needle tip location.

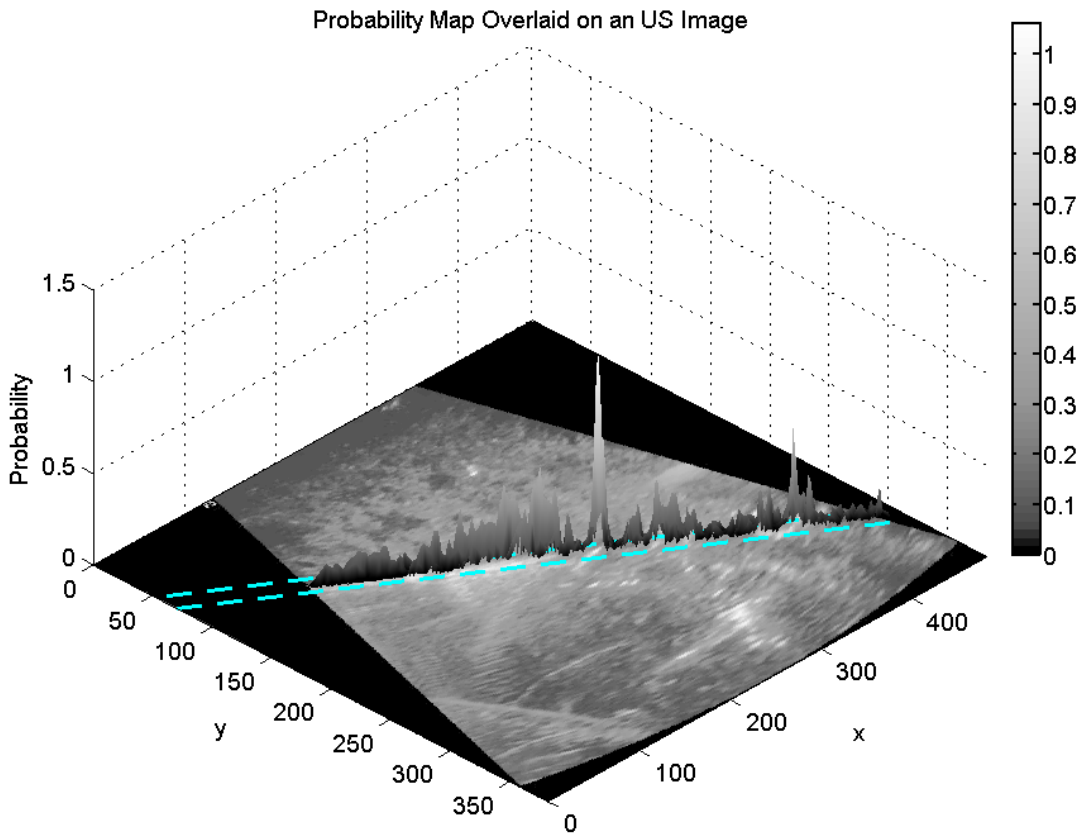

Figure 20: Three dimensional probability map of the needle's tip overlaid on the two dimensional US image that is given in Fig. 19-(a).

CHAPTER V

REAL-TIME NEEDLE TIP LOCALIZATION

This chapter presents needle tip tracking in 2D US images using Gabor filter. The needle is inserted manually, and the needle tip is tracked using 2D US imaging. The needle tip estimation noise is reduced with Kalman filter. Also, in order to test the system with imaging faults and tissue deformations, needle tip tracking simulations are performed. Tissue deformation model is used to make the simulation more realistic. Using the simulation, Kalman filter accuracy is tested and optimum noise covariance and measurement noise covariance matrices for Kalman filter are determined. This chapter also presents bin packing method to accelerate the proposed needle localization method. Using bin packing method, the processing time is reduced by 56% without a GPU so the proposed localization method executes in real-time.

5.1 Kalman Filter for Smoothing Estimation Noise

The geometrical shape of the needle is very close to a straight line in 2D US images. In real time, there can be fluctuations in the estimated needle tip trajectory because of the estimation noise coming from the algorithm explained above. The estimation noise originates from varying needle tip visibility and the alignment errors formed between the US probe's imaging plane and the needle.

In 2D US images, the visibility of the tip of the needle can be low, or the tip might be seen as an independent structure from the needle. In these situations, the needle tip is detected with an estimation error. However, if there is a misalignment, the estimation noise can be high. The point where the needle intersects the US image plane is estimated as the needle tip during misalignment occurrences. Also, the needle can disappear completely, or the needle cannot be detected by the RANSAC in the

image. As a result, the needle tip cannot be estimated. A Kalman filter is used to smoothen the estimation noise and estimate the position of the needle tip when the needle axis is not detected. Fig. 21 shows implementation of the Kalman Filter. The 2D position (x, y) and linear velocities $(\dot{x}, \dot{y})$ of the target are chosen as states for the Kalman Filter and it is described by

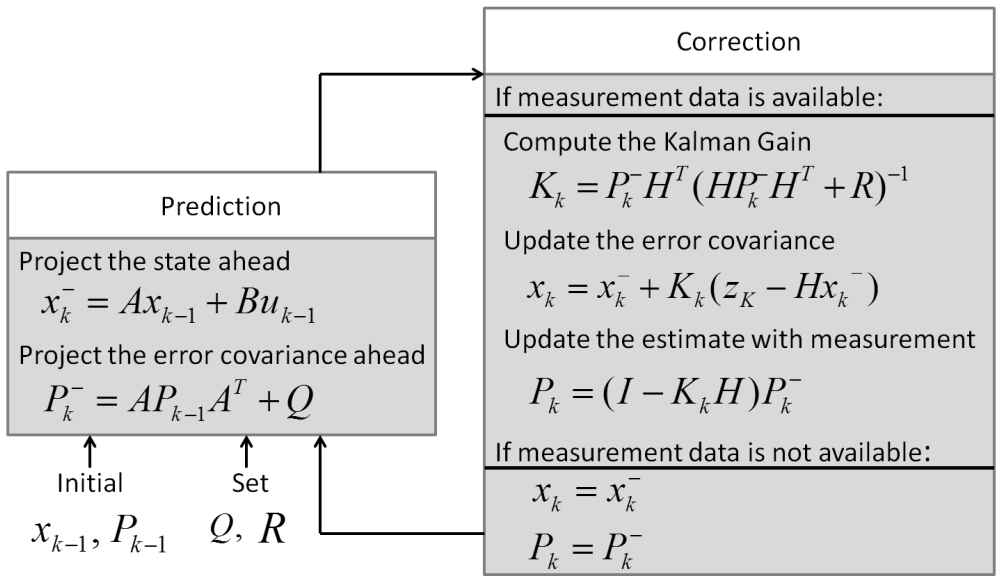

Figure 21: Kalman Filter Implementation [59]

$$x_t = \begin{bmatrix} x & y & \dot{x} & \dot{y} \end{bmatrix}^T$$

Using the states, dynamic model of the system x_k and the measurement model z_k can be formed as:

$$x_k = Ax_{k-1} + w_k,$$

$$z_k = Hx_k + v_k,$$

where

$$A = \begin{bmatrix} 1 & 0 & dt & 0 \\ 0 & 1 & 0 & dt \\ 0 & 0 & 1 & 0 \\ 0 & 0 & 0 & 1 \end{bmatrix} \quad and \quad H = \begin{bmatrix} 1 \\ 1 \\ 0 \\ 0 \end{bmatrix} \tag{34}$$

The process noise (w_k) and the measurement noise (v_k) are assumed to be zero mean Gaussian distributions with $\sim N(0, Q)$ and $\sim N(0, R)$ respectively. Q and R are the noise covariance and the measurement noise covariance matrices. These matrices are set manually and they are related to the Kalman filter performance. The results of needle tip tracking in agar-gelatin based phantom using Kalman filter are shown in 22. In order to evaluate the Kalman filter performance in realistic conditions and to obtain optimum values for the Q and R matrices, a simulation for the needle tip tracking is developed. The simulation is explained in detail in the following section.

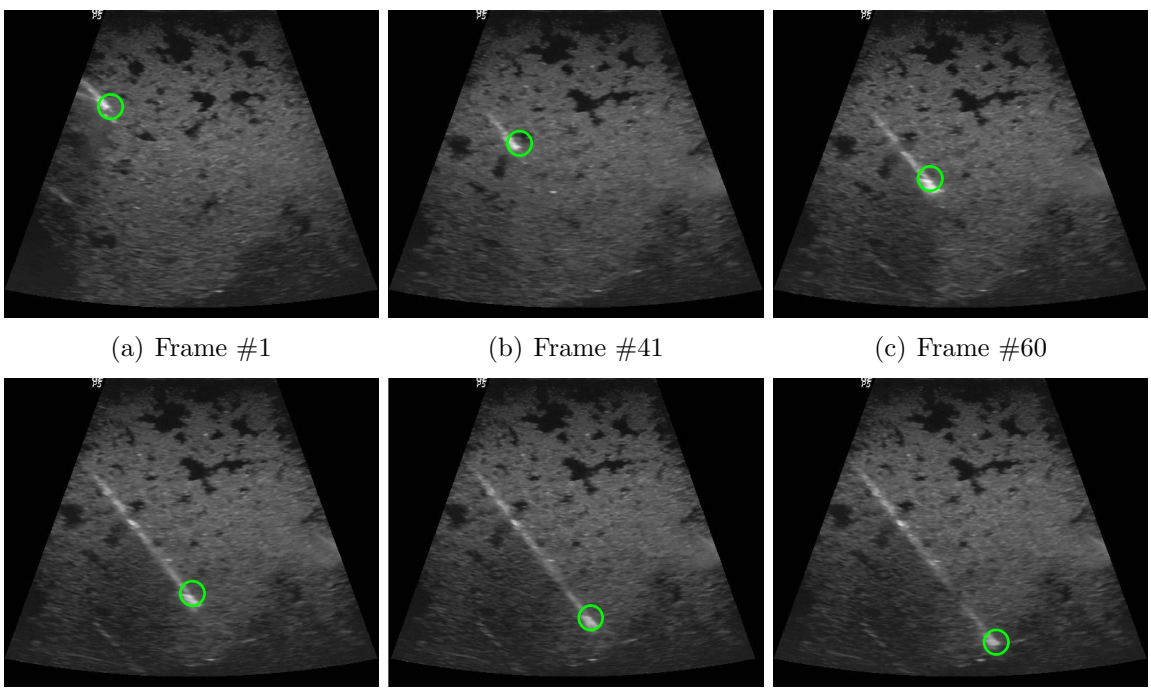

(a) Frame #1 (b) Frame #41 (c) Frame #60

(d) Frame #86 (e) Frame #100 (f) Frame #115

Figure 22: Results of the proposed needle tip localization algorithm when time step (dt) equals 0.2 seconds. The estimated needle tip location is represented using 'o'.

5.2 Needle Tip Tracking Simulation

The US images inherently are noisy. Developing new algorithms to improve needle tip localization can be slow or complicated. Hence, a simulation platform is implemented to develop localization algorithms rapidly. Also, a simulation platform would be more effective to test different conditions of the system. For instance, the misalignment between the needle and the US image plane cannot be easily tested. The main purpose of the simulation is to improve the Kalman filter performance under different types of needle tip measurement noises. In order to simulate the needle tip tracking more realistically, tissue deformations and time-to-time image plane misalignments are incorporated. In Fig. 23, needle insertion and needle retraction are simulated. Misalignment cases of the needle and the tissue deformations are also illustrated. The needle tip estimation error versus time including the simulation steps shown in Fig. 23 are plotted in Fig. 24.

Input parameters for the simulation are: (i) The location of the target, (ii) The needle insertion angle, (iii) Width of the needle region of interest, (iv) The needle motion model, (v) The noise model of the needle tip measurement, (vi) The modulus of elasticity and the Poisson's ratio of the tissue, (vii) Applied force, and (viii) Simulation time step (dt). Output parameters for the simulation are: (i) Deformed mesh with respect to dt, and (ii) The error of the Kalman filter.

A virtual spring model was used to model the tissue deformation by [60]. In our simulations, the tissue assumed to be homogenous, and made of linearly elastic material [61]. While the needle is inserted with applied force ($F_{applied}$), the tissue resists the motion in the opposite direction. The reaction force causes the tissue's internal damping ($F_{damping}$) and stiffness ($F_{stiffness}$) forces. The total force applied to the needle tip to cut the tissue ($F_{cutting}$) is described by [62] [63]

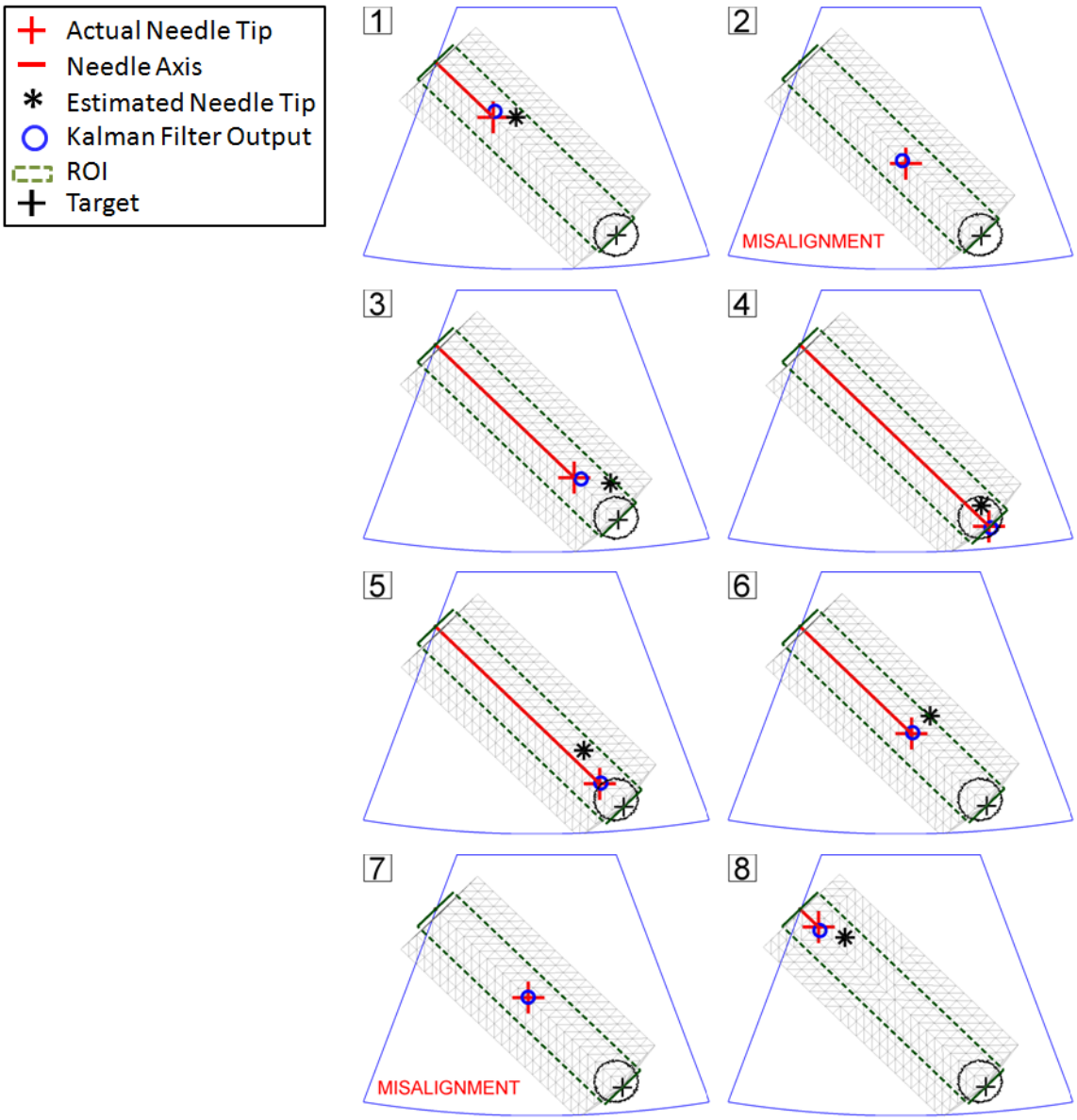

Figure 23: Simulation snapshots of the needle tip tracking are shown. The needle insertion ROI is drawn with dashed lines. For this configuration 11x24 2D-nodes are created, the width of the meshes equals two times the needle insertion ROI. The tissue is not rigid. The circular region indicates suspicious region, and the '+' in the region indicates the target. The linear line in the needle insertion ROI indicates the needle, and the actual tip of the needle is shown using '+'. The estimated needle tip and the Kalman filter output are represented using '*' and 'o', respectively. Misalignment states are indicated by labels, and the needle is not visible. As it is shown with snapshots, the Kalman filter can estimate the position of the needle tip when it is not visible.

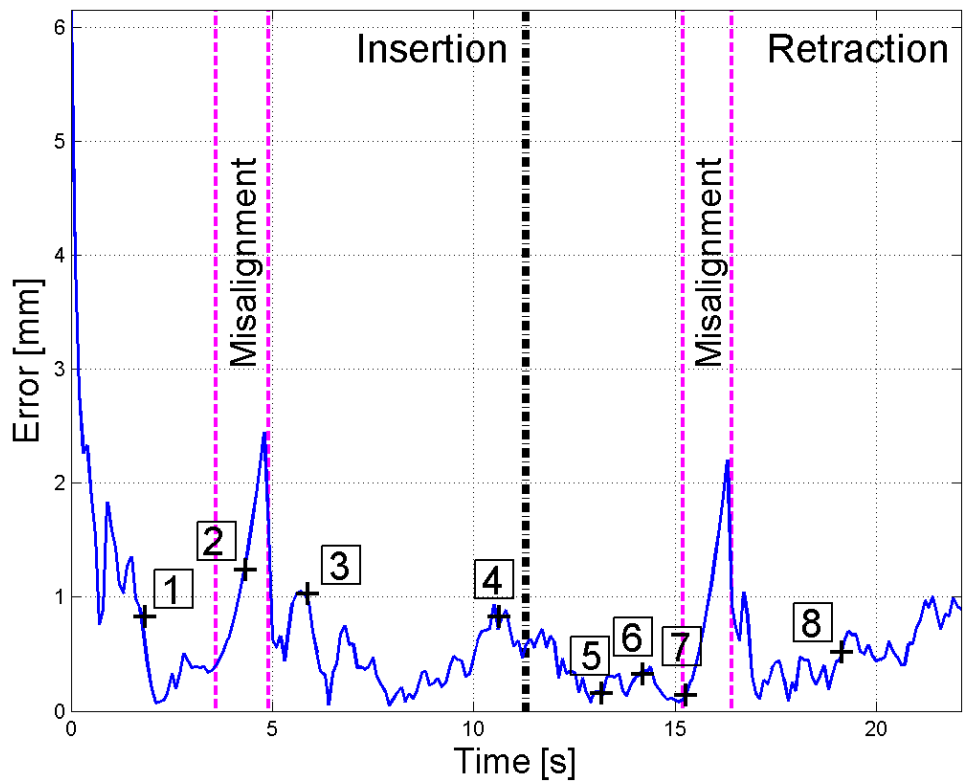

Figure 24: Needle tip estimation error versus time. The error of each frame illustrated in Fig. 23 is marked with '+' and the corresponding frame number is indicated.

$$F_{cutting} = F_{applied} - F_{stiffness} - F_{damping} \tag{35}$$

$$Ma_t = F_{applied} - Ku_t - Cv_t \tag{36}$$

where M, C and K are the mass, damping and stiffness matrices, respectively. a_t, v_t and u_t are the acceleration, velocity and position of the nodes at time t. The next position of the nodes (u_{t+1}) can be calculated as follows:

$$u_{(t+1)} = u_t + v_t dt + \frac{a_t dt^2}{2} \tag{37}$$

In our simulations, a rotated rectangular ROI is created according to the needle insertion angle and the target location (Fig. 23). The nodes are created using equal spaces and the nodes are triangulated using the Delaunay triangulations. In Figure 25, 2D 7x7 nodes are created and the figure shows the structural deformation while the needle is inserted into the tissue.

The Kalman filter performance is tested in realistic conditions using the simulation platform. Also, its performance with respect to different R and Q matrices is evaluated to obtain the optimum values. In real-time needle localization estimation, the noise is smoothened by obtaining the Kalman's R and Q matrices from the simulation.

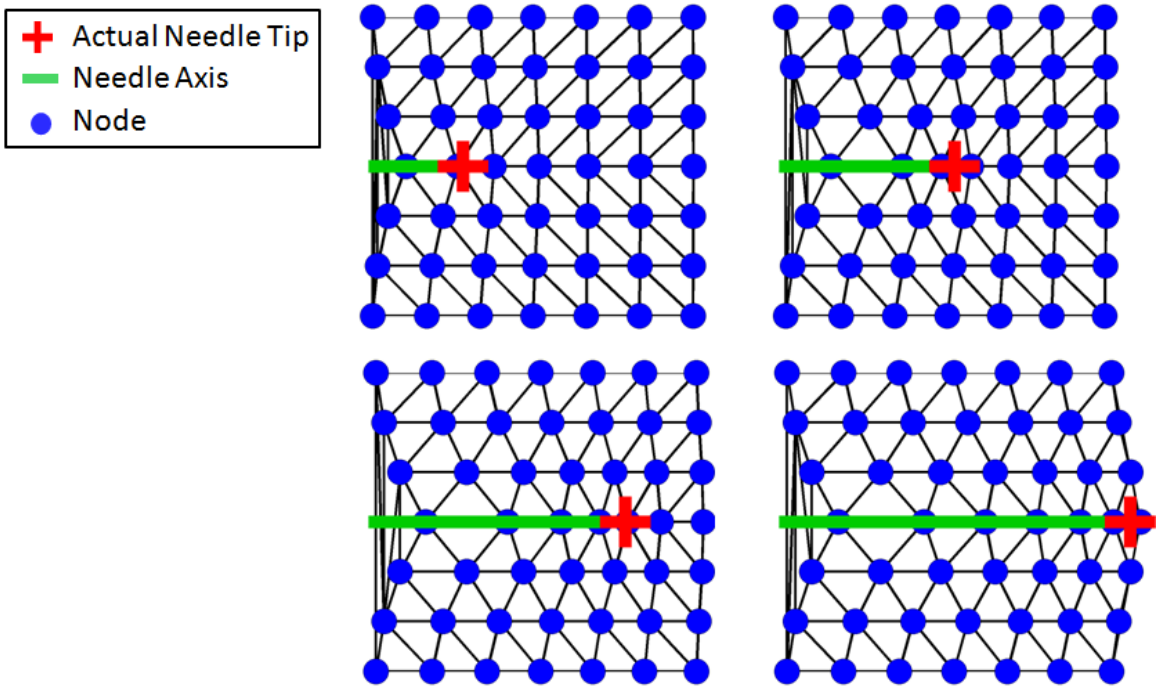

Figure 25: Snapshots of the tissue deformation while the needle is inserted. 2D 7x7 nodes are created and shown with circles. The needle axis is shown using a linear line, and the '+' indicates its actual tip position.

5.3 Bin Packing

In order to execute the proposed needle tip localization method in real time, its processing time should be decreased significantly. The proposed needle localization algorithm is fairly complex, and consists of twelve main processing steps. During the localization, the frames are processed sequentially, since each processing step depends on the previous one's output. Also, partitioning the images into sub-images and processing these in parallel is not a good way to speed up the process, because

the needle structure may not be detected, and combining these sub-images increases computational time. Hence, speeding up the processing time for a remarkable amount for single images is difficult. However, the frame sequences can be processed in parallel by applying the bin packing method to speed up the process.

The bin packing method divides the operations into equal time intervals and the processes are packed into bins. The processes in the bins are applied to different frames sequentially in separate threads. Each thread starts to process with a new incoming frame as the processes in the first bin are completed. The schematic representation of the sequential and bin packing methods are illustrated in Fig. 26. In this study, the processing time of the method's steps are measured (Table 3), and accordingly the method is divided into four bins (P1, P2, P3, and P4) with respect to their processing times. It is assumed that the processing time of each bin is approximately equal to each other, T/4 at best. If a single image is processed at a time, in T time, the needle tip is localized in Frame #1 in thread #1. However, if bin packing is used, the needle tip is localized in a thread, and that thread starts to work on the next frame. With bin packing, the needle tip is localized in four consecutive frames in 1.75T time at best, while four frames can be analyzed using a sequential processing method in 4T time.

A pipeline is a structure under which the execution of the instructions by a CPU is divided into several stages, with the operation to progress along the various units responsible for processing each stage. As a result, it is possible to start executing the next instruction without waiting for the execution of the preceding one to be completed, so the program execution can be accelerated. The bin packing method reduces the processing time by 56% at best using CPU efficiently. This is true if the images are supplied faster than the single image processing time. This value was calculated by finding the difference between 4T and 1.75T, then dividing the result of this substraction by 4T. If the proposed needle localization processes with the bin

packing method, the needle tip can be localized in real-time without needing a GPU.

	Process	Process Time (ms)	Bin
$\#1^{st}$ Stage	Image Read	2.51 ± 0.41	P1
	Gabor Filter	0.92 ± 0.18	
	Median Filter	7.43 ± 1.22	
	Otsu Thresholding	0.42 ± 0.09	P2
	Parameter Tuning	1.98 ± 0.39	
	Morphological Opr.	0.10 ± 0.02	
	RANSAC Line Fitting	3.99 ± 0.55	
$\#2^{nd}$ Stage	Gabor Filter	0.31 ± 0.05	P3
	Median Filter	7.25 ± 1.13	
	Otsu Thresholding	0.31 ± 0.06	P4
	Parameter Tuning	1.70 ± 0.21	
	Needle Tip Estimation	3.31 ± 0.34	
	Overall Processing Time	35.01 ± 3.04	

Table 3: Processing time of each process in Fig. 26. $\#1^{nd}$ and $\#2^{nd}$ stages are as in Fig. 9

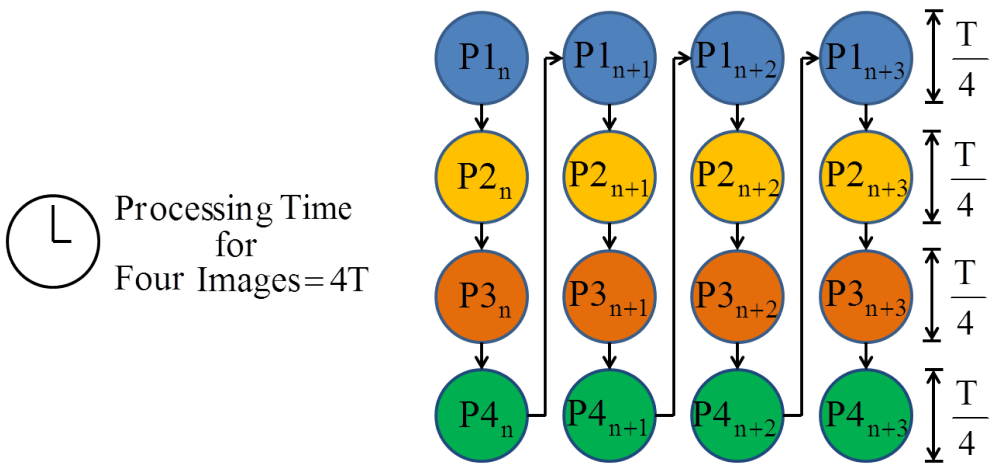

(a) Sequential processing method

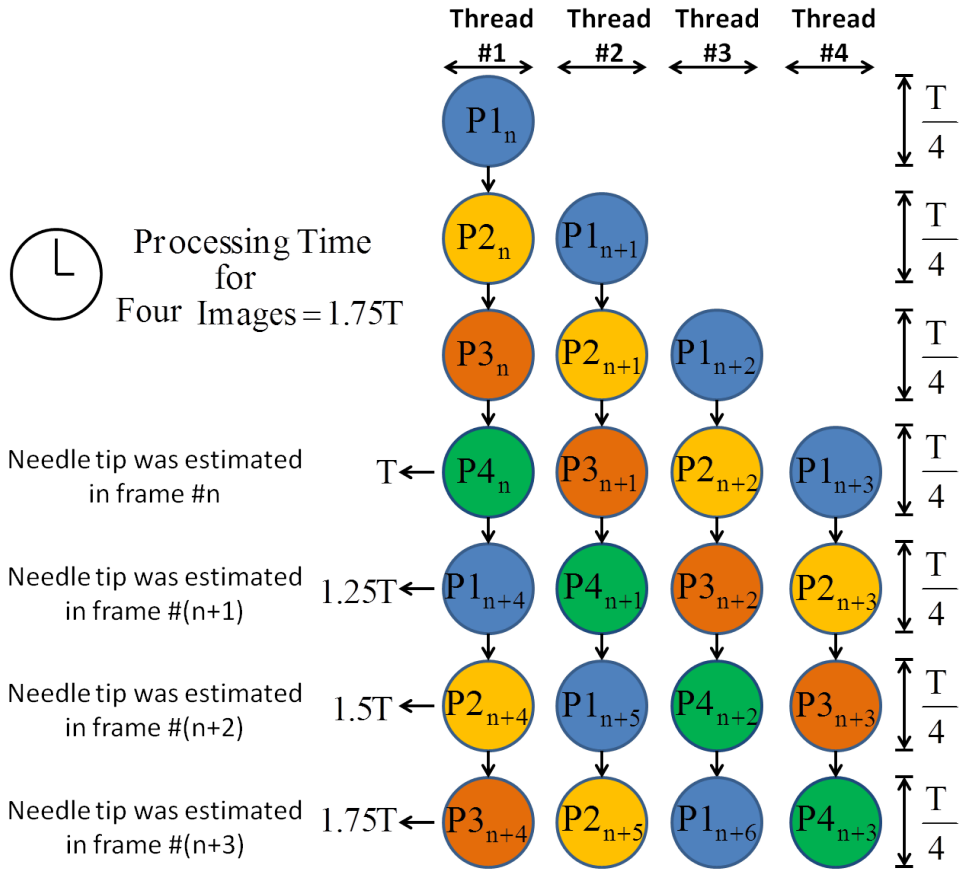

(b) Bin packing method

Figure 26: Schematic representations of sequential and bin packing methods. Processing time of each bin (T/4) is assumed to be equal to each other. At the best case, the processing time of the localizing needle tip in four frames with (a) sequential and (b) bin packing methods are $4T$ and $1.75T$, respectively. Notice that processing time of the needle localization in the first frame is equal in two methods.

CHAPTER VI

EXPERIMENTAL RESULTS

In this chapter, the accuracy of the needle insertion angle and the needle tip estimation methods are evaluated using an optical tracking system. Firstly, experimental setup are described for locating the needle tip in 2D US images and measuring the angle between US probe and the needle. Then, the execution time of the proposed localization method is given. Finally, RMS errors of the needle insertion angle and the needle tip estimation methods are presented.

6.1 Experimental Setup

6.1.1 Biopsy Robot - OBR

The robotic system that was used to insert needles is called OzU Biopsy Robot (OBR), and it has 5-DOF (see Fig. 27). It is designed to conduct biopsies on humans. The OBR consists of 3 main stages: front stage, back stage and the syringe mechanism. The front stage has 2-DOF and consists of one stationary base and four moving links attached to it. Motors are attached to the base in order to keep the moving parts light. A gimbal with 2-DOF is connected with 45° to the end-effector of the 5 bar linkage. The gimbal is used as guidance for the needle. The design of the back stage is similar to the front stage with an addition of rotational axis. A 2-DOF gimbal which carries the syringe mechanism is connected with 45° to the end-effector of the links, hence the position of the syringe mechanism according to the base of the robot can be easily calculated using kinematic equations [64]. The syringe mechanism is designed to get tissue samples from human body after the insertion of the needle.

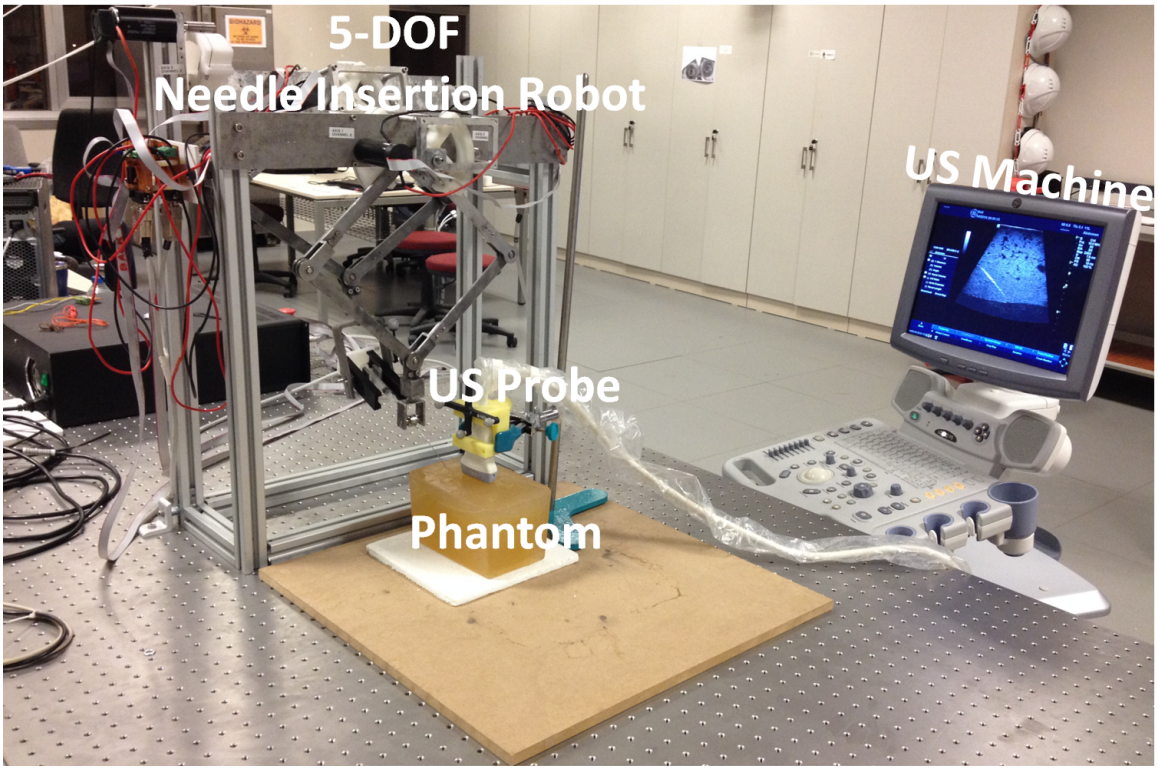

Figure 27: View of 2D US guided 5-DOF robotic system for percutaneous needle procedures.

6.1.2 US Machine

The images were acquired using a LOGIQ P5 2D US machine (General Electric, USA), with a linear 2D US probe (11L, General Electric, USA). The acquired images were 640 × 480 pixels. The images were captured from the US machine with EURESYS PICOLA HD 3G frame grabber.

6.1.3 Phantom

Four different types of phantoms and distilled water were used during needle insertion experiments. These are distilled water (@25°C), distilled water and ethanol mixture (@25°C), gelatin-based, agar-based, and gelatin and agar mixture phantoms. These phantoms were prepared according to the recipes given in Chapter III. In the experiments, STERIKING R41 22G x 15cm biopsy needles (WIPAK MEDICAL) were used.

6.1.4 Execution Time

The needle localization algorithm presented in Chapter IV was implemented in C++ using the OpenCV library, and run on a 64-bit Window 7 workstation, which has an Intel Xeon E5-2620 CPU running at 2 GHz and 32 GB of RAM. The execution time of the proposed needle axis localization and needle tip estimation in Section 4.4 for a single image is 17.00 ± 2.03 ms and 12.95 ± 1.54 ms (mean $\pm$ standard deviation), respectively.

112 frames were used to measure the processing time of the sequential and the bin packing methods mentioned in Chapter 5, Section 3. Fig. 28 shows the processing time of the sequential and the bin packing methods as histogram plot. The execution time of localizing the needle tip in a frame with sequential and the bin packing methods is 35.01 ± 3.04 ms, 13.28 ± 3.30 ms (mean $\pm$ standard deviation), respectively. Therefore, the bin packing method reduces the processing time by 56%.

Also, execution time of the algorithm without entropy based parameter tuning for a single image is in C++ 46.05 ± 3.30 ms (mean $\pm$ standard deviation). Therefore, the entropy based parameter tuning method reduces the execution time by 24%.

6.2 Needle Localization Results

6.2.1 Simulation Results

The needle tip tracking accuracy was initially evaluated with a simulation study. OBR inserts the needle with a PD controller, so in the simulation the needle tip reaches the target using PD controller. In the simulation dt was set to 50 ms and the duration of the needle insertion and the retraction are assumed to be equal. This simulation was repeated 50 times and 11100 frames were evaluated. In each frame, white Gaussian noise was added to actual needle tip location to simulate needle tip estimation noise. The noise in the needle tip estimation was smoothen using Kalman filter (see Fig. reffig:Insertion). The parameters of Kalman filter (noise covariance

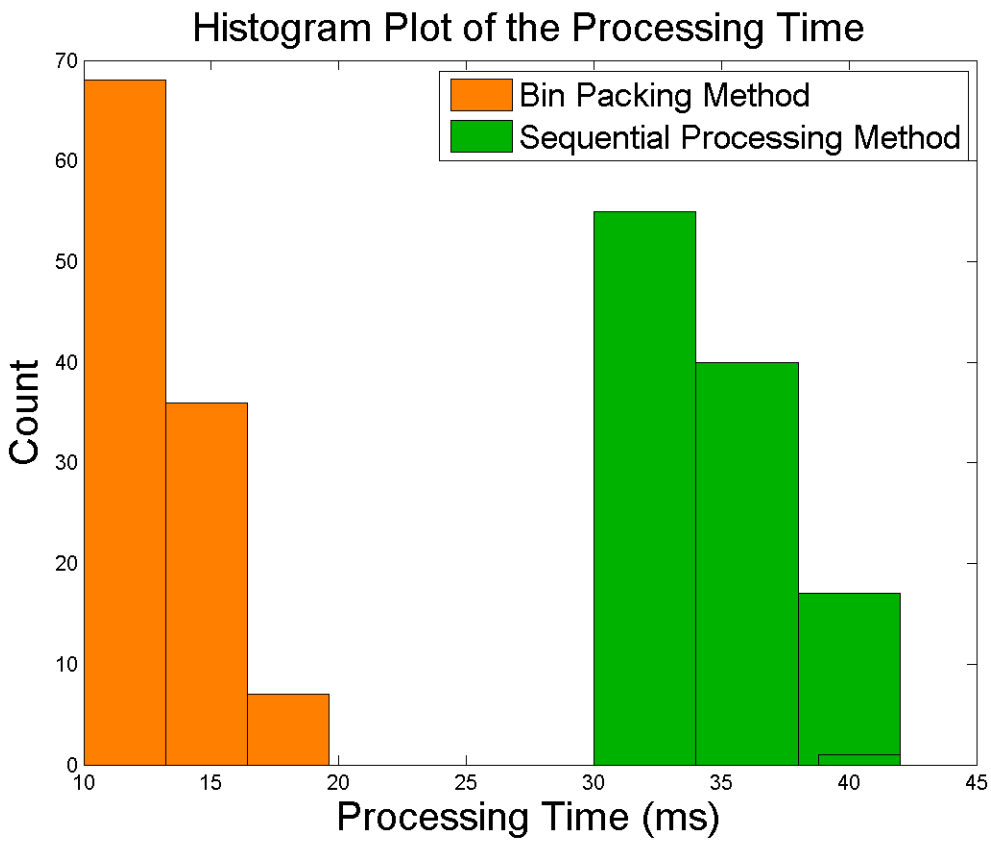

Figure 28: Processing time of the sequential and the bin packing methods

and the measurement noise covariance matrices) were tuned to get minimum and maximum error of the proposed tracking error. The minimum and maximum RMS error in the simulations of the proposed tracking method in Section 5.2 are 0.25 mm and 0.84 mm, respectively.

6.2.2 Experimental Results

The accuracy of the needle insertion angle estimation and the needle tip localization methods were evaluated using the OptiTrack optical motion capture system. 11.4 mm diameter optical markers were attached to the ultrasound probe and the needle. In order to find the needle tip position in 2D US image using motion capture, the system was calibrated with the proposed system in [65]. The needle was inserted to the agar-gelatin based phantom manually. After the needle was inserted, the angle

value and the tip position were measured both by the optical tracking system and the proposed estimation method simultaneously.

54 2D single US images were used to evaluate the accuracy of the proposed insertion angle estimation in Section 4.2.1. The RMS error of the method is 2.29°. 38 images were used to evaluate the accuracy of the needle tip localization. In order to find the error of the proposed method in Section 5.2, the Euclidean distance between the actual needle tip location and the estimated needle tip location were calculated for each frame. The RMS error of the proposed localization method is 1.17 mm.

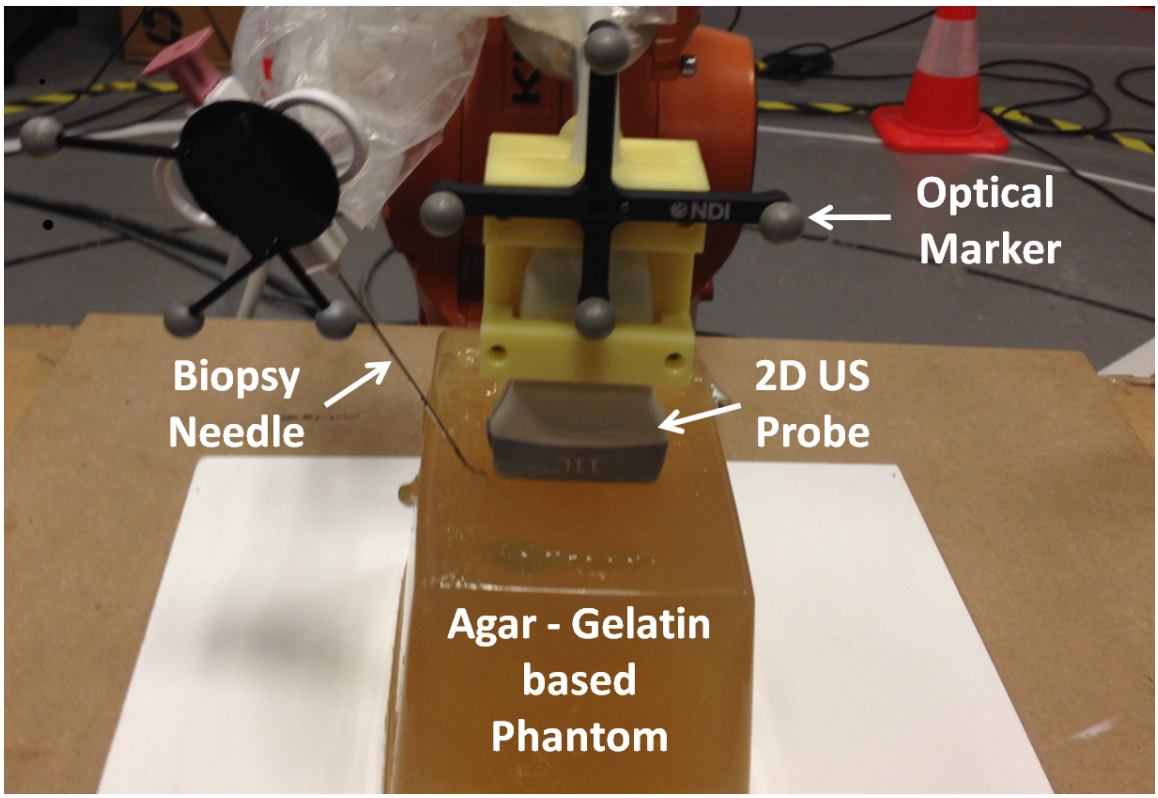

Figure 29: Experimental setup. Optical markers were attached to the needle and the US probe for position validation.

In this thesis, four different types of phantoms and a water medium were used to evaluate the algorithm capability to localize the needle axis and its tip in different contrast levels. Realistic phantoms were used specifically to prove that the proposed method works in a variety of US images with distinct backgrounds. 20 phantoms

in total were used in the experiments. The needle was inserted into each phantom at least 30 times and approximately 3 US images were captured in each insertion. In total, 1417 single 2D US images from different types of phantoms were used to evaluate the algorithm. In all of the images, the needle trajectory and its tip were localized successfully. The algorithm was able to localize the biopsy needle axis and its tip in all of phantoms confirming the robustness of the method.

CHAPTER VII

CONCLUSION

In this thesis, a needle localization method in 2D US images is proposed. The needle trajectory and the needle insertion angle are estimated without using an external sensor. The major difference of the proposed method compared to others in the literature is segmenting the needle pixels with a Gabor filter, which can distinguish the needle from the background image. This filter enhances the tubular structures in the direction of the needle insertion path filtering out the orthogonal structures. As a result, the needle pixels become brighter compared to the image background and the needle stands out.

The proposed localization method consists of the two consecutive stages. In the first stage, the Gabor filter is applied to image, then the needle insertion angle is estimated, and the needle trajectory is found with a RANSAC line estimator. In the second stage, Gabor filter is repeated, and then the needle tip location is estimated with probability mapping method. The probability of each pixel being a needle tip is calculated and the pixel with maximum probability is located as needle tip.

The proposed localization method also binarizes the US image using an entropy based parameter tuning method. Images from different types of backgrounds are binarized automatically with an optimum threshold value. The robustness of the algorithm is increased, and also the processing time is reduced by 24%.

In real-time, Kalman filter is used to smooth the needle tip estimation noise and to estimate the needle tip when the needle axis is not detected. In order to, calculate the Kalman filter accuracy under the tissue deformation and misalignment between US probe and the needle, needle tip tracking simulation is presented. Thanks to the

simulation, optimum noise covariance and the measurement noise covariance matrices are determined. In order to execute proposed method in real-time, the bin packing method is used and the processing time is reduced by 56%, without a GPU.

The proposed localization method was tested in different phantoms. In the experiments, phantoms were produced to specifically mimic the human soft tissue. In Chapter III, tissue mimicking materials and phantom preparation methods are detaily explained. Also, their acoustical properties are presented. The references mentioned in this chapter are complete and provide a survey on US phantoms.

When the experimental results are evaluated, the accuracy and speed of the proposed method is sufficient enough to be used in actual percutaneous procedures in real time. It is also necessary to note that the RMS error of the optical tracking system in position and angle measurements were 1 mm and 1°, respectively. Accuracy results of the proposed method are in the same amount of the external sensor's accuracy, which shows that the proposed needle localization method works properly.

The proposed localization method was developed for needle localization in 2D US images. However, the method capable of localizing the biopsy needles in the CT and fluoroscopy images. In these images, the needle especially its tip is very distinguishable. Also, the needle is seen as a complete structure and the intensity of the needle pixels are very high compared to anatomical structures and the image background. On the other hand, the needle visibility is very low in the US images and the needle tip can be seen as unbounded structure from needle axis in US images. The proposed method localizes the needle axis and its tip when the images contain excessive number artifacts and the intensity of needle pixels are close to the image background. Also, the algorithm was tested using close to 1500 single 2D US images from different types of phantoms. In all of the images, the needle and its tip is localized successfully. CT and fluoroscopy images do not have undesirable artifacts and reverberation effects. Hence, the needle in these images can be localized using

the proposed localization method. All in all, the proposed method can considered as framework for needle localization in the medical images.

Bibliography

[1] L. Liberman, M. Drotman, E. A. Morris, L. R. LaTrenta, A. F. Abramson, M. F. Zakowski, and D. D. Dershaw, "Imaging–histologic discordance at percutaneous breast biopsy," *Cancer*, vol. 89, no. 12, pp. 2538–2546, 2000.

[2] M. Kaya and O. Bebek, "Needle localization using gabor filtering in 2D ultrasound images," in *Proceedings of the IEEE International Conference on Robotics and Automation (ICRA)*, May 2014.

[3] M. Kaya and O. Bebek, "Gabor filter based localization of needles in ultrasound guided robotic interventions," in *IEEE International Conference on Imaging Systems and Techniques (IST)*, October 2014.

[4] M. Kaya, E. Senel, A. Ahmad, O. Orhan, and O. Bebek, "Real-time needle tip localization in 2D ultrasound images for robotic biopsies," in *IEEE International Conference on Advanced Robotics (ICAR)*, July 2015.

[5] K. J. Draper, C. C. Blake, L. Gowman, D. B. Downey, and A. Fenster, "An algorithm for automatic needle localization in ultrasound-guided breast biopsies," *Medical Physics*, vol. 27, no. 8, pp. 1971–1979, 2000.

[6] M. Ding and A. Fenster, "A real-time biopsy needle segmentation technique using hough transform," *Medical Physics*, vol. 30, no. 8, pp. 2222–2233, 2003.

[7] S. Cheung and R. Rohling, "Enhancement of needle visibility in ultrasound-guided percutaneous procedures," *Ultrasound in Medicine and Biology*, vol. 30, no. 5, pp. 617 – 624, 2004.

[8] M. Barva, J. Kybic, J. Mari, C. Cachard, and V. Hvalac, "Automatic localization of curvilinear object in 3D ultrasound images," in *SPIE International Symposium Medical Imaging*, Feb 2005.

[9] M. Barva, J. Kybic, J. Mari, C. Cachard, and V. Hvalac, "Localizing metal electrode from 3D ultrasound data using r-ransac and intensity priors," in *EMBEC'05*, 2005.

[10] S. H. Okazawa, R. Ebrahimi, J. Chuang, R. N. Rohling, and S. E. Salcudean, "Methods for segmenting curved needles in ultrasound images," *Medical Image Analysis*, vol. 10, no. 3, pp. 330 – 342, 2006.

[11] P. M. Novotny, J. A. Stoll, N. V. Vasilyev, P. J. del Nido, P. E. Dupont, and R. D. Howe, "Gpu based real-time instrument tracking with three dimensional ultrasound," in *Proceedings of the 9th international conference on Medical Image Computing and Computer-Assisted Intervention - Volume Part I*, pp. 58–65, 2006.

[12] J. Stoll, H. Ren, and P. Dupont, "Passive markers for tracking surgical instruments in real-time 3-D ultrasound imaging," *Medical Imaging, IEEE Transactions on*, vol. 31, no. 3, pp. 563–575, 2012.

[13] H. Neshat and R. Patel, "Real-time parametric curved needle segmentation in 3D ultrasound images," in *Biomedical Robotics and Biomechatronics (BIOROB), 2nd IEEE RAS EMBS International Conference on*, pp. 670–675, 2008.

[14] M. Fronheiser, S. Idriss, P. Wolf, and S. Smith, "Vibrating interventional device detection using real-time 3-D color doppler," *Ultrasonics, Ferroelectrics and Frequency Control, IEEE Transactions on*, vol. 55, no. 6, pp. 1355–1362, 2008.

[15] T. K. Adebar and A. M. Okamura, "3D segmentation of curved needles using doppler ultrasound and vibration," in *Information Processing in Computer-Assisted Interventions*, pp. 61–70, Springer, 2013.

[16] B. Dong, E. Savitsky, and S. Osher, "A novel method for enhanced needle localization using ultrasound-guidance," in *Advances in Visual Computing*, pp. 914–923, Springer, 2009.

[17] M. Uhercik, J. Kybic, C. Cachard, and H. Liebgott, "Line filtering for detection of microtools in 3D ultrasound data," in *Ultrasonics Symposium (IUS), IEEE International*, pp. 594–597, 2009.

[18] Y. Zhao, A. Bernard, C. Cachard, and H. Liebgott, "Biopsy needle localization and tracking using roi-rk method," in *Abstract and Applied Analysis*, Hindawi Publishing Corporation, 2014.

[19] A. Frangi, W. Niessen, K. Vincken, and M. Viergever, "Multiscale vessel enhancement filtering," in *Medical Image Computing and Computer-Assisted Interventation MICCAI98*, vol. 1496, pp. 130–137, Springer Berlin Heidelberg, 1998.

[20] M. Aboofazeli, P. Abolmaesumi, P. Mousavi, and G. Fichtinger, "A new scheme for curved needle segmentation in three-dimensional ultrasound images," in *Proceedings of the Sixth IEEE international conference on Symposium on Biomedical Imaging: From Nano to Macro*, ISBI'09, pp. 1067–1070, 2009.

[21] X. Wen, S. Salcudean, and P. Lawrence, "Detection of brachytherapy seeds using 3D transrectal ultrasound," *Biomedical Engineering, IEEE Transactions on*, vol. 57, pp. 2467–2477, Oct 2010.

[22] A. Ayvaci, P. Yan, S. Xu, S. Soatto, and J. Kruecker, "Biopsy needle detection in transrectal ultrasound," *Computerized Medical Imaging and Graphics*, vol. 35, pp. 653 – 659, 2011.

[23] K. Cao, D. Mills, and K. Patwardhan, "Automated catheter detection in volumetric ultrasound," in *Biomedical Imaging (ISBI), 2013 IEEE 10th International Symposium on*, pp. 37–40, April 2013.

[24] G. Vrooijink, M. Abayazid, and S. Misra, "Real-time three-dimensional flexible needle tracking using two-dimensional ultrasound," in *Proceedings of the International Conference on Robotics and Automation (ICRA)*, no. 2, pp. 1680–1685, IEEE Robotics and Automation Society, May 2013.

[25] P. Chatelain, A. Krupa, and M. Marchal, "Real-time needle detection and tracking using a visually served 3D ultrasound probe," in *International Conference on Robotics and Automation (ICRA)*, no. 2, pp. 1668–1673, IEEE Robotics and Automation Society, May 2013.

[26] M. Renfrew, Z. Bai, and M. Cavusoglu, "Particle filter based active localization of target and needle in robotic image-guided intervention systems," in *Automation Science and Engineering (CASE), 2013 IEEE International Conference on*, pp. 448–454, Aug 2013.

[27] K. Mathiassen, D. Dall Alba, R. Muradore, P. Fiorini, and O. Elle, "Real-time biopsy needle tip estimation in 2D ultrasound images," in *Proceedings of International Conference on Robotics and Automation (ICRA)*, no. 2, pp. 4348–4353, IEEE Robotics and Automation Society, May 2013.

[28] P. Beigi and R. Rohling, "Needle localization using a moving stylet/catheter in ultrasound-guided regional anesthesia: a feasibility study," in *SPIE Medical Imaging*, pp. 90362Q–90362Q, International Society for Optics and Photonics, 2014.

[29] R. O. Bude and R. S. Adler, "An easily made, low-cost, tissue-like ultrasound phantom material," *Journal of clinical ultrasound*, vol. 23, no. 4, pp. 271–273, 1995.

[30] R. W. Prager, R. Rohling, A. Gee, and L. Berman, "Rapid calibration for 3-D freehand ultrasound," *Ultrasound in medicine and biology*, vol. 24, no. 6, pp. 855–869, 1998.

[31] G. A. Bellingham and P. W. Peng, "A low-cost ultrasound phantom of the lumbosacral spine," *Regional anesthesia and pain medicine*, vol. 35, no. 3, pp. 290–293, 2010.

[32] L. Wee, E. Supriyanto, and W. Mahmud, *Ultrasound Image Processing: and its Application using Matlab*. Lambert Academic Publishing, 2011.

[33] M. O. Culjat, D. Goldenberg, P. Tewari, and R. S. Singh, "A review of tissue substitutes for ultrasound imaging," *Ultrasound in Medicine and Biology*, vol. 36, no. 6, pp. 861 – 873, 2010.

[34] T. Kondo, M. Kitatuji, and H. Kanda, "New tissue mimicking materials for ultrasound phantoms," in *Ultrasonics Symposium, 2005 IEEE*, vol. 3, pp. 1664–1667, 2005.

[35] L. M. Cannon, A. J. Fagan, and J. E. Browne, "Novel tissue mimicking materials for high frequency breast ultrasound phantoms," *Ultrasound in medicine and biology*, vol. 37, no. 1, pp. 122–135, 2011.

[36] M. Vatandas, A. Koc, and C. Koc, "Ultrasonic velocity measurements in ethanol-water and methanolwater mixtures," *European Food Research and Technology*, vol. 225, no. 3-4, pp. 525–532, 2007.

[37] N. Bush and C. Hill, "Gelatine-alginate complex gel: A new acoustically tissue-equivalent material," *Ultrasound in Medicine and Biology*, vol. 9, no. 5, pp. 479 – 484, 1983.

[38] E. Madsen, G. Frank, T. Krouskop, T. Varghese, F. Kallel, and J. Ophir, "Tissue-mimicking oil-in-gelatin dispersions for use in heterogeneous elastography phantoms," *Ultrasonic imaging*, vol. 25, no. 1, pp. 17–38, 2003.

[39] E. L. Madsen, M. A. Hobson, H. Shi, T. Varghese, and G. R. Frank, "Tissue-mimicking agar/gelatin materials for use in heterogeneous elastography phantoms," *Physics in medicine and biology*, vol. 50, no. 23, p. 5597, 2005.

[40] R. O. Bude and R. S. Adler, "An easily made, low-cost, tissue-like ultrasound phantom material," *Journal of Clinical Ultrasound*, vol. 23, no. 4, pp. 271–273, 1995.

[41] E. L. Madsen, J. A. Zagzebski, R. A. Banjavie, and R. E. Jutila, "Tissue mimicking materials for ultrasound phantoms," *Medical physics*, vol. 5, no. 5, pp. 391–394, 1978.

[42] M. M. Burlew, E. L. Madsen, J. A. Zagzebski, R. A. Banjavic, and S. W. Sum, "A new ultrasound tissue-equivalent material.," *Radiology*, vol. 134, no. 2, pp. 517–520, 1980.

[43] M. Rowan and P. Pedersen, "P2c-3 an injury mimicking ultrasound phantom as a training tool for diagnosis of internal trauma," in *Ultrasonics Symposium, 2006.*, pp. 1612–1617, IEEE, 2006.

[44] J. W. Li, M. K. Karmakar, X. Li, W. H. Kwok, and W. D. N. Kee, "Gelatin-agar lumbosacral spine phantom a simple model for learning the basic skills required to perform real-time sonographically guided central neuraxial blocks," *Journal of Ultrasound in Medicine*, vol. 30, no. 2, pp. 263–272, 2011.

[45] J. Dang, P. Lasaygues, D. Zhang, S. Tavernier, N. Felix, B. Frisch, S. Mensah, and M. Wan, "Development of breast anthropomorphic phantoms for combined pet-ultrasound elastography imaging," in *Nuclear Science Symposium Conference Record (NSS/MIC), 2009 IEEE*, pp. 3088–3092, IEEE, 2009.

[46] E. L. Madsen, G. R. Frank, and F. Dong, "Liquid or solid ultrasonically tissue-mimicking materials with very low scatter," *Ultrasound in medicine & biology*, vol. 24, no. 4, pp. 535–542, 1998.

[47] S. R. Stauffer and N. A. Peppast, "Poly (vinyl alcohol) hydrogels prepared by freezing-thawing cyclic processing," *Polymer*, vol. 33, no. 18, pp. 3932–3936, 1992.

[48] S. L. Vieira, T. Z. Pavan, J. E. Junior, and A. A. Carneiro, "Paraffin-gel tissue-mimicking material for ultrasound-guided needle biopsy phantom," *Ultrasound in Medicine and Biology*, vol. 39, no. 12, pp. 2477 – 2484, 2013.

[49] L. Maggi, M. von Kruger, W. Pereira, and E. Monteiro, "Development of silicon-based materials for ultrasound biological phantoms," in *Ultrasonics Symposium (IUS), IEEE International*, pp. 1962–1965, 2009.

[50] J. Sheppard and F. Duck, "Ultrasonic tissue-equivalent materials using inorganic gel mixtures," 1982.

[51] I. Fogel and D. Sagi, "Gabor filters as texture discriminator," *Biological Cybernetics*, vol. 61, no. 2, pp. 103–113, 1989.

[52] C.-J. Lee and S.-D. Wang, "Fingerprint feature extraction using gabor filters," *Electronics Letters*, vol. 35, no. 4, pp. 288–290, 1999.

[53] C. Vicas, M. Lupsor, R. Badea, and S. Nedevschi, "Detection of anatomical structures on ultrasound liver images using gabor filters," in *Automation Quality and Testing Robotics (AQTR), 2010 IEEE International Conference on*, vol. 2, pp. 1–5, 2010.

[54] R. Rangayyan, F. Oloumi, F. Oloumi, P. Eshghzadeh-Zanjani, and F. Ayres, "Detection of blood vessels in the retina using gabor filters," in *Electrical and Computer Engineering. Canadian Conference on*, pp. 717–720, 2007.

[55] N. Otsu, "A Threshold Selection Method from Gray-level Histograms," *IEEE Transactions on Systems, Man and Cybernetics*, vol. 9, no. 1, pp. 62–66, 1979.

[56] J. Kapur, P. Sahoo, and A. Wong, "A new method for gray-level picture thresholding using the entropy of the histogram," *Computer Vision, Graphics, and Image Processing*, vol. 29, no. 3, pp. 273 – 285, 1985.

[57] T. Acharya and A. Ray, *Image Processing: Principles and Applications*. Wiley, 2005.

[58] Huseyin Celik MD, "Personal communication," *Acibadem Hospital, Bursa*.

[59] G. Welch and G. Bishop, "An introduction to the kalman filter," 1995.

[60] Z. Yuan, Y. Zhang, J. Zhao, Y. Ding, C. Long, L. Xiong, D. Zhang, and G. Liang, "Real-time simulation for 3D tissue deformation with CUDA based GPU computing," *Journal of Convergence Information Technology*, vol. 5, no. 4, pp. 109–119, 2010.

[61] R. Alterovitz, K. Goldberg, J. Pouliot, R. Taschereau, and I.-C. Hsu, "Sensorless planning for medical needle insertion procedures," in *in Proceedings of the IEEE/RSJ International Conference on Intelligent Robots and Systems (IROS)*, vol. 4, pp. 3337–3343 vol.3, Oct 2003.

[62] A. M. Okamura, C. Simone, and M. D. O'Leary, "Force modeling for needle insertion into soft tissue," *Biomedical Engineering, IEEE Transactions on*, vol. 51, no. 10, pp. 1707–1716, 2004.

[63] R. Alterovitz and K. Goldberg, "Comparing algorithms for soft tissue deformation: accuracy metrics and benchmarks," *Rapport technique, UC Berkeley: Alpha Lab*, pp. 42–44, 2002.

[64] O. Bebek, M. J. Hwang, and M. Cavusoglu, "Design of a parallel robot for needle-based interventions on small animals," *Mechatronics, IEEE/ASME Transactions on*, vol. 18, pp. 62–73, Feb 2013.

[65] A. Ahmad, C. Cavusoglu, and O. Bebek, "Calibration of 2D ultrasound in 3D space for robotic biopsies," in *International Conference on Advanced Robotics (ICAR)*, 2015.